Neuron

Article

Munc13-1 is a Ca^{2+}-phospholipid-dependent vesicle priming hub that shapes synaptic short-term plasticity and enables sustained neurotransmission

Graphical abstract

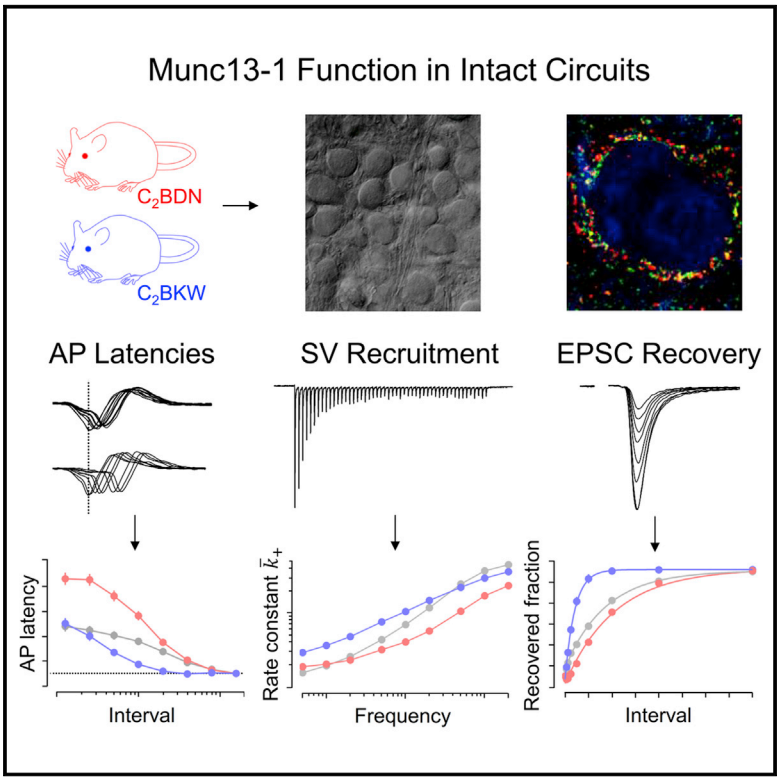

Highlights

- The Munc13-1 C_2B domain controls synaptic vesicle replenishment rates
- Blocking Ca^{2+}-phospholipid-C_2B signaling attenuates vesicle replenishment
- Enhancing Ca^{2+}-phospholipid-C_2B signaling accelerates vesicle replenishment
- This process determines short-term plasticity and fidelity of synaptic transmission

Authors

Noa Lipstein, Shuwen Chang, Kun-Han Lin, Francisco José López-Murcia, Erwin Neher, Holger Taschenberger, Nils Brose

Correspondence

htasche@gwdg.de (H.T.), brose@em.mpg.de (N.B.)

In brief

Using novel knockin mouse models, Lipstein et al. show that Ca^{2+}-phospholipid binding activates the presynaptic protein Munc13-1 to fine-tune the rate of synaptic vesicle replenishment according to synaptic activity. This process determines short-term synaptic plasticity and the temporal fidelity of synaptic transmission in the auditory brainstem and the hippocampus.

Lipstein et al., 2021, Neuron *109*, 3980–4000
December 15, 2021
https://doi.org/10.1016/j.neuron.2021.09.054

CellPress

CellPress
OPEN ACCESS

Neuron

Article

Munc13-1 is a Ca^{2+}-phospholipid-dependent vesicle priming hub that shapes synaptic short-term plasticity and enables sustained neurotransmission

Noa Lipstein,[1,6] Shuwen Chang,[1,4,5] Kun-Han Lin,[2,4] Francisco José López-Murcia,[1,4] Erwin Neher,[2,3] Holger Taschenberger,[1,*] and Nils Brose[1,3,7,*]

[1]Department of Molecular Neurobiology, Max Planck Institute of Experimental Medicine, Göttingen, Germany
[2]Emeritus Laboratory of Membrane Biophysics, Max Planck Institute for Biophysical Chemistry, Göttingen, Germany
[3]Cluster of Excellence "Multiscale Bioimaging," Georg August University, Göttingen, Germany
[4]These authors contributed equally
[5]Present address: Shenzhen Institute of Advanced Technology, Chinese Academy of Sciences, Shenzhen, China; Shenzhen-Hong Kong Institute of Brain Science-Shenzhen Fundamental Research Institutions, Shenzhen, China
[6]Present address: Leibniz-Forschungsinstitut für Molekulare Pharmakologie, Berlin, Germany
[7]Lead contact
*Correspondence: htasche@gwdg.de (H.T.), brose@em.mpg.de (N.B.)
https://doi.org/10.1016/j.neuron.2021.09.054

SUMMARY

During ongoing presynaptic action potential (AP) firing, transmitter release is limited by the availability of release-ready synaptic vesicles (SVs). The rate of SV recruitment (SVR) to release sites is strongly upregulated at high AP frequencies to balance SV consumption. We show that Munc13-1—an essential SV priming protein—regulates SVR via a Ca^{2+}-phospholipid-dependent mechanism. Using knockin mouse lines with point mutations in the Ca^{2+}-phospholipid-binding C_2B domain of Munc13-1, we demonstrate that abolishing Ca^{2+}-phospholipid binding increases synaptic depression, slows recovery of synaptic strength after SV pool depletion, and reduces temporal fidelity of synaptic transmission, while increased Ca^{2+}-phospholipid binding has the opposite effects. Thus, Ca^{2+}-phospholipid binding to the Munc13-1-C_2B domain accelerates SVR, reduces short-term synaptic depression, and increases the endurance and temporal fidelity of neurotransmission, demonstrating that Munc13-1 is a core vesicle priming hub that adjusts SV re-supply to demand.

INTRODUCTION

Neuronal signaling at chemical synapses requires transmitter release by synaptic vesicle (SV) fusion. A fraction of SVs residing at molecularly defined release sites constitutes the pool of readily releasable SVs (RRP) (Kaeser and Regehr, 2017), which are in a molecularly mature—"primed"—state to allow rapid membrane fusion upon an action potential (AP)-induced increase in cytosolic Ca^{2+} ($[Ca^{2+}]_i$). To maintain synaptic transmission during continuous activity, empty release sites must be re-populated with fusion-competent SVs (SV recruitment [SVR]).

SVR is generally slow, with a time constant of several seconds (Fuhrmann et al., 2004; Pyott and Rosenmund, 2002; Stevens and Tsujimoto, 1995; von Gersdorff et al., 1997; Wesseling and Lo, 2002), but can be transiently accelerated by an order of magnitude following bouts of synaptic activity (Sakaba and Neher, 2001a; Stevens and Wesseling, 1998), most likely due to the buildup of presynaptic $[Ca^{2+}]_i$ (Dittman and Regehr, 1998; Sakaba and Neher, 2001a). This enables synapses to maintain high levels of transmitter release during presynaptic AP firing, resulting in reduced synaptic short-term depression (STD), and to speed up the recovery of synaptic strength following activity while $[Ca^{2+}]_i$ decays back to resting levels (Dittman et al., 2000; Fuhrmann et al., 2004; Wang and Kaczmarek, 1998). By counteracting SV pool depletion, the SVR speed is a key determinant of synaptic strength and short-term plasticity (STP) and affects multiple complex brain processes (Zucker and Regehr, 2002).

Because $[Ca^{2+}]_i$ controls several steps of the SV cycle and regulates numerous Ca^{2+}-binding proteins (for review, see Alabi and Tsien, 2012 and Neher and Sakaba, 2008), the identity of proteins that mediate activity-dependent SVR acceleration has remained enigmatic. Moreover, beyond their $[Ca^{2+}]_i$ sensitivity, SVR-regulating pathways also respond to lipid second messengers. During activity, the presynaptic membrane lipid composition changes as a consequence of SV fusion and the activity of lipid-modifying enzymes, some of which are Ca^{2+} regulated. In neuroendocrine cells, for example, vesicle fusion occurs at membrane sites rich in PIP_2 (phosphatidylinositol-4,5-bisphosphate) and PIP_2 augments RRP replenishment (Kabachinski et al., 2014; Milosevic et al., 2005; Walter et al., 2017). PIP_2 conversion to diacylglycerol (DAG) regulates transmitter release in cultured neurons (Rhee et al., 2002; Wierda et al., 2007) and *in situ* (Lou et al., 2008; Malenka et al., 1987).

The present study was designed to demonstrate a Ca^{2+}- and phospholipid-controlled step in SVR and STP regulation. We focused on the SV priming protein Munc13-1, a presynaptic active zone (AZ) component that is essential for transmitter release (Augustin et al., 1999b; Varoqueaux et al., 2002). Munc13-1 operates by regulating the conformation of the soluble N-ethylmaleimide-sensitive-factor attachment receptor (SNARE) fusion protein syntaxin, thus promoting partial SNARE complex formation and close SV-plasma membrane contact (Imig et al., 2014; Lai et al., 2017; Ma et al., 2011). The Munc13-1 MUN domain, which mediates SV priming, is located downstream of three regulatory domains: a Ca^{2+}-calmodulin (Ca^{2+}-CaM) binding motif (Junge et al., 2004; Lipstein et al., 2012a, 2013; Piotrowski et al., 2020) a DAG-binding C_1 domain (Betz et al., 1998), and a C_2 domain (C_2B) that binds phospholipids in a Ca^{2+}-dependent manner (Michelassi et al., 2017; Shin et al., 2010). These regulatory domains profoundly affect Munc13-1 activity *in vitro* (Junge et al., 2004; Rhee et al., 2002; Shin et al., 2010). However, a block of CaM binding to Munc13-1 has only subtle effects on SV priming during and after AP trains in intact circuits (Lipstein et al., 2013), demonstrating that major signaling pathways involved in SVR regulation are still unknown. In this context, the C_2B domain of Munc13-1 is an excellent candidate, as Munc13-1 is indispensable for SV priming in most synapses, is localized at the AZ membrane, and can sense Ca^{2+} and membrane phospholipids via its C_2B domain.

To examine the role of the Munc13-1 C_2B domain in Ca^{2+}- and phospholipid-dependent SVR regulation *in situ*, we generated knockin (KI) mouse lines that express Munc13-1 variants with either abolished or increased Ca^{2+} and phospholipid binding to the C_2B domain (Shin et al., 2010) and characterized functional consequences in the calyx of Held synapse. We demonstrate that presynaptic activity activates Munc13-1 by Ca^{2+}-phospholipid binding to its C_2B domain. This causes distinctly higher SVR rates and thus shapes STP, enables sustained transmission, and enhances the temporal fidelity of synaptic signaling.

RESULTS

Generation of Munc13-1 C_2BDN and C_2BKW KI mice

The Ca^{2+}-binding site in the Munc13-1 C_2B domain is composed of negatively charged residues that chelate Ca^{2+}, thus allowing negatively charged phospholipids to bind. We exchanged two such aspartic acid residues by asparagine (D705N and D711N) to create the Munc13-1 C_2BDN KI line (Shin et al., 2010). This exchange abolishes Ca^{2+} binding, slightly increases phospholipid binding at low [Ca^{2+}] (likely due to less membrane repulsion), and abolishes Ca^{2+}-mediated phospholipid binding at high [Ca^{2+}] (Shin et al., 2010). To increase the C_2B domain affinity to phospholipids, we created the Munc13-1 C_2BKW KI, targeting a lysine (K706) in the outer rim of the Ca^{2+}-binding site. In the synaptotagmin-1 (Syt1) C_2A domain, the corresponding residue is large and hydrophobic (M173), inserts into membrane bilayers, and enhances Ca^{2+}-dependent phospholipid binding (Chapman and Davis, 1998; Gerber et al., 2002; Shin et al., 2010; Zhang et al., 1998). We replaced K706 with tryptophan (K706W), which increases PIP_2 binding without changing the Ca^{2+} affinity of the C_2B domain (Shin et al., 2010; Figures 1A–1D).

Homozygous mutant (mut) KIs of both lines were viable and fertile but showed an ~30% body weight reduction at 2 weeks of age (Figure 1E), which did not persist. Neither KI line showed signs of distress or gross behavioral abnormalities. Analyses of expression levels of a selected set of presynaptic proteins did not reveal any genotype-related differences (Figures 1F and S1A–S1C). The localization of the mutant Munc13-1 variants in presynaptic compartments contacting principal neurons (PNs) of the medial nucleus of the trapezoid body (MNTB) was examined by immunostaining (Figure S1D). A similar typical pattern of Munc13-1-positive structures co-localizing with the AZ marker Bassoon and surrounding MNTB PN somata was observed in wild-type (WT) and KI samples (Figures S1D–S1F; Chen et al., 2013; Lipstein et al., 2013).

In sum, we generated two novel KI mouse lines with specific point mutations in the Munc13-1 C_2B domain that abolish (C_2BDN) or increase (C_2BKW) Ca^{2+}-dependent phospholipid binding without altering Munc13-1 expression or localization.

Basal transmission and presynaptic Ca^{2+} influx in Munc13-1 C_2BDN and C_2BKW synapses

To assess the role of the Munc13-1 C_2B domain in synaptic transmission and STP, we used the calyx of Held synapse, as it is accessible to pre- and postsynaptic recordings (Borst et al., 1995; Forsythe, 1994). Recordings were obtained from homozygous mut and WT littermates (mut_{DN} and WT_{DN} for C_2BDN KIs; mut_{KW} and WT_{KW} for C_2BKW) at postnatal day (P) 14–P17, i.e., after hearing onset, when Munc13-1 is functionally dominant (Chen et al., 2013). Only minor differences were observed between WT_{DN} and WT_{KW} (Table S1).

To assay synaptic strength and evoked excitatory postsynaptic current (eEPSC) kinetics, we recorded unitary eEPSCs in voltage-clamped MNTB PNs (Figure 2A). Unless stated otherwise, recordings were obtained in the presence of 1 mM kynurenic acid (kyn) (STAR Methods; Figure S2). In C_2BDN mice, we observed larger eEPSCs in mut_{DN} as compared to WT_{DN} (Figures 2A–2C; Table S1), whereas in C_2BKW mice, eEPSC amplitudes were indistinguishable between mut_{KW} and WT_{KW}. eEPSC kinetics were unaltered (Figures 2B and 2C; Table S1). Scatterplots of eEPSC rise time versus eEPSC half-width revealed a positive correlation (Figure S2), reflecting a developmental eEPSC shortening (Joshi et al., 2004; Koike-Tani et al., 2005; Taschenberger and von Gersdorff, 2000). This correlation was similar in all genotypes, indicating no adverse effects of KI mutations on developmental synapse refinement.

We next measured paired-pulse ratios (*PPR*s) (*PPR* = $eEPSC_2/eEPSC_1$) of two consecutive eEPSCs evoked at interstimulus intervals (*ISI*s) of 5 ms–2 s (Figures 2D and 2E). In many synapses, including the calyx of Held (Debanne et al., 1996; Dobrunz and Stevens, 1997; Taschenberger et al., 2016), *PPR*s correlate with initial eEPSCs size, indicating that differences in synaptic strength arise, at least partly, from differences in release probability. Regression lines fitted to log-linear plots of $1 - PPR$ versus *ISI* provide estimates for average release probabilities ($\bar{p}$) and average SV pool replenishment rate constants ($\bar{k}_+$) (Betz, 1970). We observed lower *PPR*s at all *ISI*s in mut_{DN} synapses (Figure 2E1; Table S1) as compared to WT_{DN} synapses, indicative of elevated $\bar{p}$ in the former. In

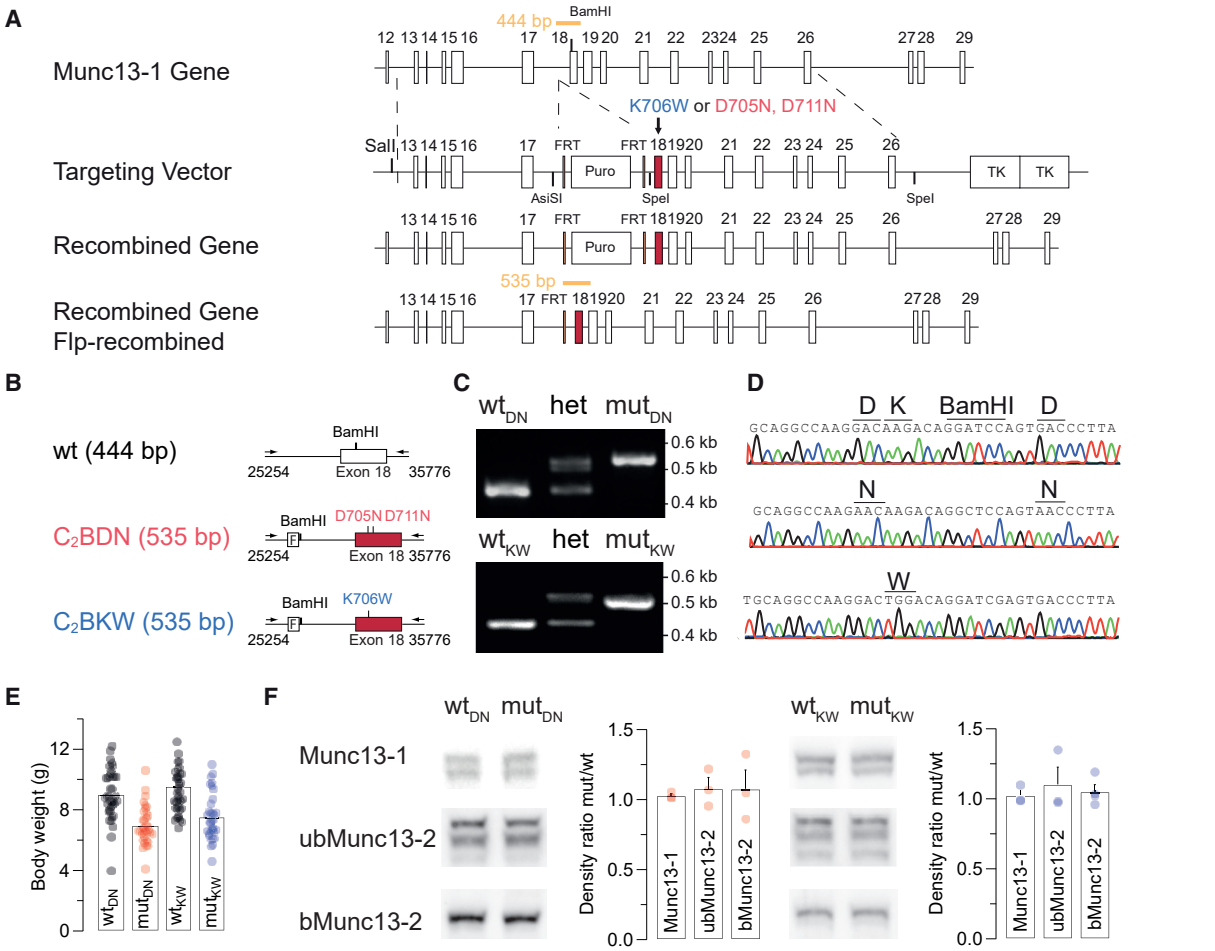

Figure 1. Munc13-1 C_2BDN and C_2BKW KI mice

(A) Munc13-1 gene, targeting vector, mutated gene after homologous recombination, and mutated gene after Flp recombination to remove the puromycin cassette. Exon 18 is indicated in red. FRT, flippase recognition target; Puro, puromycin resistance gene; TK, herpes simplex virus thymidine kinase. Puro and TK cassettes are not drawn to scale.

(B–D) Genotyping strategy for the Munc13-1 KI mice of the indicated genotypes (F, frt site).

(C) Gel electrophoresis of PCR products using mouse tail DNA of the indicated genotypes.

(D) Sequence chromatograms of the mutated region in exon 18 of the indicated genotypes.

(E) Scatter dot plots and bar graphs showing individual and average values of body weights of juvenile (P14–P17) C_2BDN (left) and C_2BKW (right) mice.

(F) Quantitative western blot analysis showing no difference in the expression levels of Munc13-1, ubMunc13-2, and bMunc13-2.

Data depict mean ± SEM. Differences among mean density values were statistically not significant ($p > 0.05$; ANOVA). See also Figure S1.

contrast, *PPRs* were similar in mut_{KW} and WT_{KW} synapses, consistent with unchanged $\bar{p}$. However, a steeper slope of the log-linear plot of $1 - PPR$ versus *ISI* indicated a faster $\bar{k}_+$ in mut_{KW} synapses (Figure 2E2).

To test whether enhanced presynaptic Ca^{2+} influx contributes to the elevated $\bar{p}$ in mut_{DN} synapses, we recorded pharmacologically isolated voltage-gated Ca^{2+} currents ($I_{Ca(V)}$) in voltage-clamped calyx terminals (Figures 2F and 2G). Peak $I_{Ca(V)}$ amplitudes were similar in mut and WT terminals, indicating similar voltage-gated Ca^{2+} channel (VGCC) densities (Figure 2G; Table S1). To assess VGCC gating kinetics, we quantified the charge of $I_{Ca(V)}$ ($Q_{Ca(V)}$) elicited by short AP-like depolarizations, assuming that altered activation or deactivation of $I_{Ca(V)}$ will affect its current integral (Figure 2F; Li et al., 2007), and detected no differences (Figure 2G; Table S1).

These data show that basal synaptic transmission is intact in C_2BDN and C_2BKW KI synapses. No indications of developmental abnormalities or postsynaptic modifications were observed, and normal eEPSC kinetics indicate unaltered SV fusion kinetics. The C_2BDN mutation leads to enhanced synaptic strength, partly due to elevated $\bar{p}$, but neither mutation alters VGCC expression or kinetics. Thus, the increased $\bar{p}$ in mut_{DN} synapses is either caused by a subtle change in AP waveform not affecting eEPSC kinetics or, more likely, by a mechanism downstream of Ca^{2+} influx that increases the apparent Ca^{2+} sensitivity of SVs in mut_{DN} terminals. The C_2BKW mutation

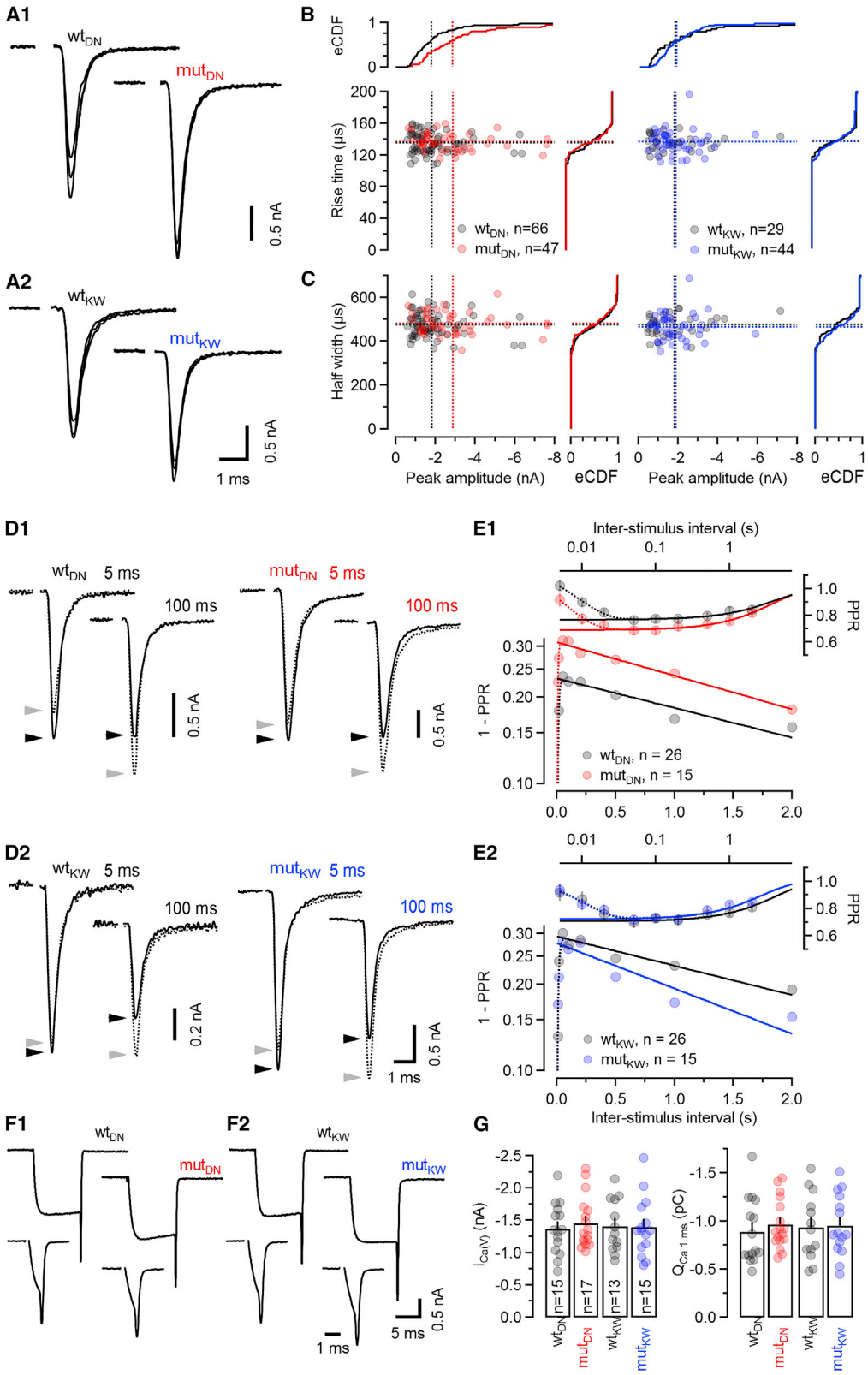

(legend on next page)

does not affect eEPSC amplitudes but accelerates the recovery from STD induced by single eEPSCs.

The Munc13-1 C_2B domain regulates steady-state rates of quantal release during repetitive synaptic stimulation

During AP trains, calyx of Held synapses typically show STD at low and intermediate (<50 Hz) stimulus frequencies (f_{stim}) and sometimes transient facilitation followed by STD at higher f_{stim} ($\geq$50 Hz; Grande and Wang, 2011; Taschenberger et al., 2016). Quantal release at steady state is limited by the SVR rate. To examine the role of the Munc13-1 C_2B domain in determining STD, we recorded eEPSC trains for a range of f_{stim} (0.5–200 Hz, 35 APs; Figures 3A1 and 3A2). Normalized average eEPSC train amplitudes showed stronger STD at high f_{stim} for mut_{DN} as compared to WT_{DN} synapses (Figure 3B1; Table S1), whereas reduced STD was seen for all but the highest f_{stim} in mut_{KW} as compared to WT_{KW} synapses (Figure 3B2; Table S1).

The relationship between steady-state quantal release and f_{stim} is illustrated in Figure 3C by plotting $eEPSC_{ss}$ and average steady-state release ($eEPSC_{ss} \times f_{stim} = \bar{r}_{-} \times q$, where $\bar{r}_{-}$ and q are the average release rate and quantal size, respectively) against f_{stim}. $eEPSC_{ss}$ was larger in mut_{DN} as compared to WT_{DN} synapses for all $f_{stim} \leq 10$ Hz. This is likely a consequence of only minor SV pool depletion during such low-frequency trains, so that $eEPSC_{ss}$ largely reflects the higher $\bar{p}$ in mut_{DN}. In contrast, for $f_{stim} \geq 20$ Hz, $eEPSC_{ss}$ and $\bar{r}_{-} \times q$ were smaller in mut_{DN} as compared to WT_{DN} synapses, indicating that slower SVR limits the amount of release in the former (Figure 3C). In mut_{KW} synapses, a different picture emerged: for all but the three highest frequencies (50, 100, and 200 Hz), $EPSC_{ss}$ and $\bar{r}_{-} \times q$ were larger in mut_{KW} as compared to WT_{KW} synapses. Because $eEPSC_1$ and $\bar{p}$ are similar in mut_{KW} and WT_{KW} synapses (Figure 2), this is consistent with a faster SVR in mut_{KW} at $f_{stim} \leq$ 20 Hz (Figure 3C).

As SVR enhancement at high firing rates is thought to be mediated by AP-evoked presynaptic Ca^{2+} influx (Dittman and Regehr, 1998; Wang and Kaczmarek, 1998), and as Munc13-1 mutations were reported to affect VGCC behavior in cultured neurons (Calloway et al., 2015), we tested whether presynaptic Ca^{2+} influx is altered in Munc13-1 C_2B KI calyces by examining frequency-dependent modulation of calyceal $I_{Ca(V)}$ during trains of AP-like depolarizations. Neither magnitude nor time course of $I_{Ca(V)}$ or its frequency-dependent facilitation was different between mut and WT terminals (Figures 3D and 3E; Table S1).

These data lead to the conclusion that the C_2BDN mutation slows SVR preferentially for higher f_{stim} while the C_2BKW mutation accelerates SVR preferentially for lower f_{stim}. This causes reduced steady-state release during high-frequency trains in mut_{DN} and enhanced steady-state release during low frequency trains in mut_{KW} synapses.

The number of readily releasable SVs is not altered in Munc13-1 C_2BDN and C_2BKW synapses

Given the key role of Munc13-1 in RRP establishment and maintenance (Augustin et al., 1999b; Varoqueaux et al., 2002), we next tested whether the C_2BDN and C_2BKW mutations affect the RRP. Pool size estimates corresponding to the subpool of "fast releasing" SVs (*FRP*) (Sakaba, 2006) were obtained from cumulative eEPSC amplitudes measured during high-frequency trains and corrected for ongoing SVR (Schneggenburger et al., 1999; Figure 4A). An estimate for $\bar{p}$ is obtained from the ratio $eEPSC_1/FRP$. *FRP* estimates increased and $\bar{p}$ values decreased with increasing f_{stim}, likely because of more complete pool depletion (Figures 4A and 4B). We therefore termed these estimates FRP' and $\bar{p}'$. When plotting $1/FRP'$ and $\bar{p}'$ versus *ISI*, we observed a roughly linear relationship between these quantities and ISI. Assuming this relationship holds for the entire *ISI* range, we obtained corrected estimates for pool size (FRP_{corr}) and release probability ($\bar{p}_{corr}$) by extrapolation to *ISI* = 0 s. FRP_{corr} values were slightly larger when comparing C_2BDN and C_2BKW mut with littermate WT synapses (Figure 4B; Table S1) but statistically not significantly different, although $\bar{p}_{corr}$ was significantly higher in mut_{DN} synapses (Figure 4B; Table S1), consistent with their larger initial eEPSCs and reduced *PPR* (Figures 2C and 2E1).

To exclude the possibility of an overcorrection when estimating FRP_{corr}, we performed three controls. (1) Assuming a simple SV pool depletion model, an estimate for release probability can be obtained by plotting eEPSC amplitudes during high-frequency trains versus the cumulative sum of previous eEPSCs (Elmqvist and Quastel, 1965; Neher, 2015). Such plots show steeper negative slopes for mut_{DN} as compared to WT_{DN} synapses, consistent

Figure 2. Amplitudes, kinetics, and paired-pulse ratios of unitary AP-evoked EPSCs

Unitary AP-evoked EPSCs (eEPSCs) were elicited by fiber stimulation and recorded in voltage-clamped principal neurons (PNs) of the MNTB.

(A) eEPSCs recorded in C_2BDN (A1) and C_2BKW (A2) calyx synapses. Three consecutive eEPSCs obtained from WT (left) and mut (right) littermates are shown superimposed.

(B and C) Scatter graphs of eEPSC rise times (B) and eEPSC half-widths (C) plotted versus eEPSC peak amplitudes. Empirical cumulative probability density functions (eCDFs) are shown on top and to the right for eEPSC amplitudes and rise times and half-widths, respectively.

(D and E) Paired-pulse ratios (PPRs) for inter-stimulus intervals (ISIs) 5 ms–2 s.

(D) eEPSC pairs recorded in C_2BDN (D1) and C_2BKW (D2) calyx synapses of WT (left) and mut (right) littermates. Solid traces with peaks marked by black arrowheads represent $EPSC_2$; dotted traces with peaks marked by gray arrowheads represent $EPSC_1$.

(E) Average data for *PPR* (top) or 1 − *PPR* (bottom) plotted against ISI. Dotted traces represent fits to the experimental data using a simple model accounting for synaptic depression and facilitation (STAR Methods). Solid traces represent the same fit but with the facilitation term removed. In a log-linear plot of 1 − *PPR* against ISI (bottom), the y-intercept and slope of the solid traces represent estimates for $\bar{p}$ and replenishment rate constant, respectively (Betz, 1970).

(F and G) Presynaptic $I_{Ca(V)}$ elicited by step-depolarizations from −80 to 0 mV in voltage-clamped calyces.

(F) $I_{Ca(V)}$ recorded in the same terminals in response to steps of either 10-ms (top) or 1-ms (bottom) duration in C_2BDN (F1) and C_2BKW (F2) calyces of WT (left) and mut (right) littermates.

(G) Bar graphs and scatter dot plots representing average values and individual terminals, respectively, of presynaptic $I_{Ca(V)}$ peak amplitudes measured during 10-ms steps (left) and $Q_{Ca(V)}$ measured during 1-ms steps (right).

Data depict mean ± SEM; n values and statistical significance are summarized in Table S1. See also Figure S2.

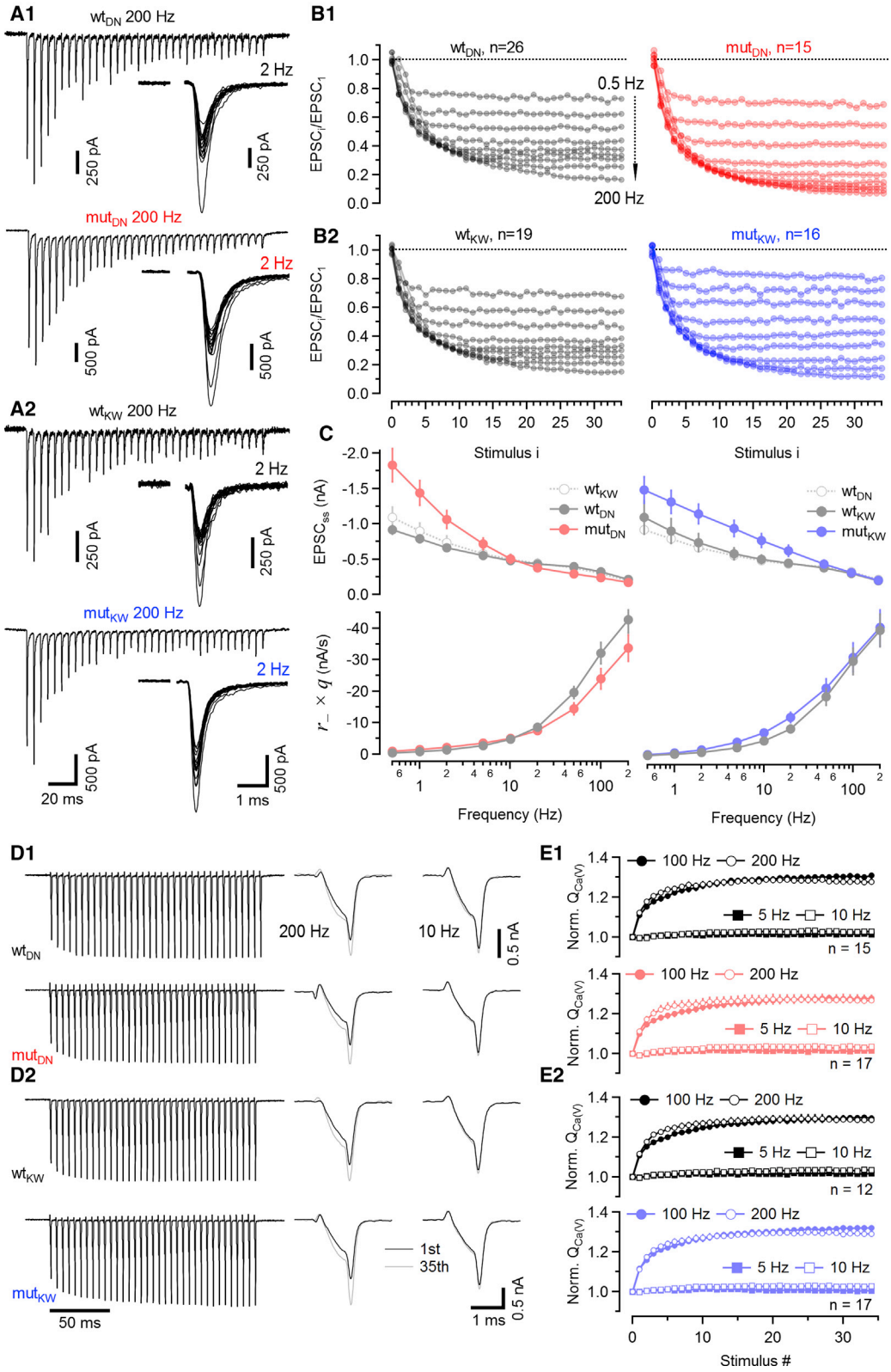

(legend on next page)

with more rapid SV consumption and therefore higher $\bar{p}$ in the former (Figure S3A1). In contrast, slopes and, therefore, $\bar{p}$ estimates were similar in WT_{KW} and mut_{KW} synapses (Figure S3A2). Both findings confirm our earlier conclusions (Figure 4B). (2) For a second set of control experiments, we recorded 200-Hz eEPSC trains in WT synapses before and after bath application of tetraethylammonium (TEA), a blocker of voltage-gated potassium channels that broadens calyceal APs and increases AP-evoked Ca^{2+} influx and $\bar{p}$ (Ishikawa et al., 2003; Figure S3B), and observed an apparent *FRP* increase of ~40% in the presence of TEA. This is in accord with the average ratio between FRP_{corr} and $FRP'_{200\ Hz}$ in both WT_{DN} and also WT_{KW} synapses (Figure S3C), indicating that our strategy to correct *FRP* estimates for incomplete pool depletion (Figure 4B) does not result in a substantial overestimate. (3) Finally, we assayed SV fusion by measuring ΔC_m in response to depolarizing voltage steps of incrementing duration in voltage-clamped calyces. ΔC_m-based pool estimates do not rely on postsynaptic responses and thus are not susceptible to AMPA receptor (AMPAR) saturation or desensitization. However, long-lasting presynaptic depolarizations—during which presynaptic $[Ca^{2+}]_i$ spatially equilibrates—trigger release from an additional subpool of "slowly releasing" SVs (*SRP*; Sakaba and Neher, 2001b), while during short and spatially restricted AP-evoked $[Ca^{2+}]_i$ elevations, SVs of the *SRP* fuse to a much lesser extent (Sakaba, 2006). Increasing $I_{Ca(V)}$ duration led to larger ΔC_m (Figure 4C). The average relationship between quantal release and Ca^{2+} influx duration was very similar in WT and mutant C_2BDN or mutant C_2BKW calyces with respect to both ΔC_m amplitudes and release kinetics (Figure 4D; Table S1). Despite the caveat that ΔC_m represents the sum of fast and slowly releasing SVs (*FRP* + *SRP*), these experiments do not reveal changes in SV pool size in mut_{DN} or mut_{KW} synapses.

These data show that the Munc13-1 C_2BDN and C_2BKW mutations do not affect the number of release-ready SVs in calyx terminals. Thus, changes in SV pool size are unlikely to contribute to the observed differences in steady-state release rates and STP.

Munc13-1 C_2BDN and C_2BKW mutations change the average rate constants of SV recruitment

Knowing steady-state release rates and the total number of release-ready SVs in resting calyces allowed us to approximate the relationship between f_{stim} and the average *FRP* replenishment rate constant ($\bar{k}_+$), which represents the rate of release site refilling per empty site averaged over one inter-stimulus interval. Figure 4E plots $\bar{k}_+$ versus f_{stim} for WT and C_2B mutant synapses. For WT_{DN} and WT_{KW} synapses, a similar relationship between $\bar{k}_+$ and f_{stim} was observed (Figure 4E1). At the highest f_{stim} of 200 Hz, $\bar{k}_+$ is >10-fold above its value estimated for f_{stim} = 0.5 Hz. The reciprocal of the maximum $\bar{k}_+$ of ~4 s^{-1} ($\tau = \frac{1}{\bar{k}_+} \approx$ 250 ms) agrees well with the rapid time constant of *FRP* replenishment measured following prolonged presynaptic depolarizations (τ_1 = 270 ms, Lipstein et al., 2013; τ_1 = 360 ms, Sakaba and Neher, 2001a). Figure 4E shows that the C_2BDN and C_2BKW mutations alter the relationship between $\bar{k}_+$ and f_{stim} so that the dynamic range of $\bar{k}_+$ is reduced. However, in mut_{DN} synapses, we observed a decreased $\bar{k}_+$ for all $f_{stim} \geq 2$ Hz as compared to WT values (Figure 4E2). In contrast, higher $\bar{k}_+$ values were estimated for all stimulation frequencies $\leq$20 Hz in mut_{KW} synapses (Figure 4E2).

These data demonstrate lower SVR rate constants for mut_{DN} synapses mainly at high f_{stim} and higher SVR rate constants for mut_{KW} synapses for low and intermediate f_{stim}, consistent with the changes observed during steady-state depression.

Abolishing Ca^{2+} binding to the Munc13-1 C_2B domain eliminates a fast component of eEPSC recovery following high-frequency conditioning

Having established that Munc13-1 C_2B mutations alter $\bar{k}_+$ during ongoing stimulation, we next tested eEPSC recovery after conditioning trains. When calyces are conditioned with low-frequency trains, eEPSCs recover with a slow time course that is well described by a single exponential ($\tau \approx 4$ s; Iwasaki and Takahashi, 2001; von Gersdorff et al., 1997). Upon high-frequency conditioning, an additional fast recovery component is observed at calyces (Wang and Kaczmarek, 1998) and other synapses (Cho et al., 2011; Gomis et al., 1999; Wang and Manis, 2008; Yang and Xu-Friedman, 2008). This fast recovery is presumed to depend on elevated $[Ca^{2+}]_i$, and Ca^{2+}-CaM binding to Munc13-1 participates in the molecular signaling pathway that mediates it (Lipstein et al., 2013; Sakaba and Neher, 2001a).

To examine SVR, we applied 100-Hz (25 stimuli) or 200-Hz (50 stimuli) trains to induce strong *FRP* depletion and monitored recovery of synaptic strength by measuring $eEPSC_{test}$ amplitudes at different intervals (Figure 5A1). When plotting fractional recovery ($eEPSC_{test} - eEPSC_{ss}$)/($eEPSC_1 - eEPSC_{ss}$) versus recovery interval (Figure 5A3; Table S1), we observed for WT_{DN} synapses

Figure 3. Changes in synaptic strength and presynaptic $I_{Ca(V)}$ during stimulus trains

(A) eEPSCs elicited by 200-Hz (left) and 2-Hz (right) AP trains and recorded in C_2BDN (A1) and C_2BKW (A2) calyx synapses of WT (top) and mut (bottom) littermates.

(B) $eEPSC_i/eEPSC_1$ ratios (*i* denotes stimulus number 1–35; $eEPSC_1$ represents the average amplitude of the first eEPSC for a given synapse across all f_{stim}) measured in response to stimulus trains (35 APs delivered at 0.5–200 Hz) in C_2BDN (B1) and C_2BKW (B2) mice. Mean normalized eEPSC amplitudes obtained in WT and mut littermates are shown in the left and right columns, respectively.

(C) Comparison of steady-state eEPSCs ($eEPSC_{ss}$, top row) and average steady-state release measured in nA/s ($\bar{r}_- \times q = eEPSC_{ss} \times f_{stim}$, bottom row) in C_2BDN (left panels) and C_2BKW (right panels) calyx synapses for WT and mut littermates. $eEPSC_{ss}$ was estimated by averaging the last four eEPSCs.

(D) Modulation of calyceal $I_{Ca(V)}$ during 200-Hz (left and middle panels) and 10-Hz (right panels) trains of brief depolarizations (thirty-five 1-ms steps from V_h = −80 mV to 0 mV) in C_2BDN (D1) and C_2BKW (D2) calyces. The last (gray) and the first (black) $I_{Ca(V)}$ are shown superimposed for comparison at an expanded timescale for 200- (middle panels) and 10-Hz trains (right panels).

(E) Summary data showing normalized charge of $I_{Ca(V)}$ trains elicited by 5-, 10-, 100-, and 200-Hz stimulus trains and recorded in C_2BDN (E1) and C_2BKW (E2) calyx terminals. $Q_{Ca(V)}$ values are shown in the top and bottom panels, respectively.

Data depict mean ± SEM; n values and statistical significance are summarized in Table S1.

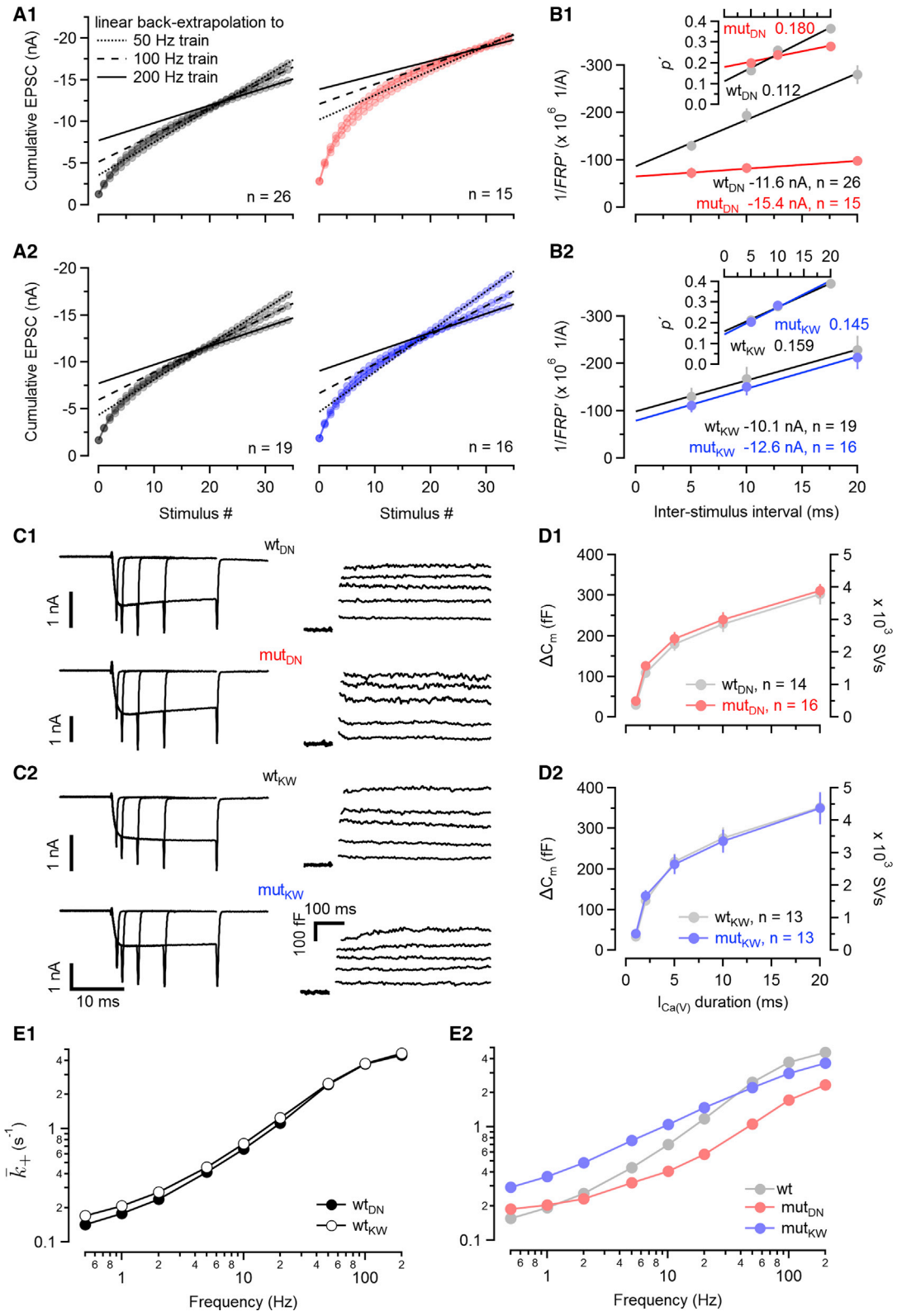

(legend on next page)

a biphasic time course requiring a fast component to account for the recovery during the initial 500 ms (Figure 5A3; Lipstein et al., 2013, their Figure 5), which was selectively and completely abolished in mut_{DN} synapses (Figures 5A2 and 5A3). After 16 s, full recovery of $eEPSC_{test}$ was seen in both mut_{DN} and WT_{DN} synapses. Closer inspection of the time course of fractional recovery revealed values slightly below zero in mut_{DN} synapses for the two shortest intervals (125 and 250 ms; Figure 5A3). This can be explained by acknowledging that release probability increases during conditioning stimulation and that this synaptic facilitation decays faster than *FRP* recovery proceeds. Such an effect is likely occluded by the fast SVR component in WT synapses but uncovered in mut_{DN} synapses that lack this SVR component.

These data show that a fast SVR component is absent in mut_{DN} synapses with abolished C_2B domain binding to Ca^{2+} and phospholipids. Because a fast SVR component is observed in WT_{DN} synapses only after high-frequency conditioning, we expected the recovery time course after 10- or 20-Hz conditioning to be largely unaltered in mut_{DN} as compared to WT_{DN} synapses. This is indeed the case (Figure S4), demonstrating that the slow component of eEPSC recovery is unaffected in mut_{DN} synapses.

Ca^{2+}-CaM binding to Munc13-1 is independent of Ca^{2+} binding to the C_2B domain

The effects of the C_2BDN mutation on SVR resemble those reported previously for a Ca^{2+}-CaM-binding-deficient Munc13-1 mutant (W464R; CaMWR; WT_{WR} and mut_{WR} for WT and mut littermates, respectively; Lipstein et al., 2013). To compare STP at C_2BDN and CaMWR calyces under identical conditions, we performed recordings similar to those described above also for WT_{WR} and mut_{WR} synapses and analyzed normalized eEPSC amplitudes during stimulus trains (Figure S5A), *FRP*, and $\overline{p}$ estimates (Figures S5B–S5D); the relationship between f_{stim} and steady-state release $(\bar{r}_{-} \times q)$; and the apparent average replenishment rate constant $\overline{k}_{+}$ (Figures S5E and S5F) for WT_{WR} and mut_{WR} synapses. While *FRP* and $\overline{p}$ estimates were unchanged, we observed lower steady-state release during high-frequency stimulation in mut_{WR} synapses, which corresponded to reduced $\overline{k}_{+}$. Accordingly, the dynamic range for $\overline{k}_{+}$ was reduced as seen for mut_{DN} synapses (Figure 4E2). As reported (Lipstein et al., 2013), we observed slower recovery after depleting stimulus trains in mut_{WR} synapses (Figures S5G1 and S5G2). However, contrary to the C_2BDN mutation and consistent with Lipstein et al. (2013), differences in the eEPSC recovery time course were less pronounced after 200- as compared to 100-Hz conditioning. The presence of residual fast SV replenishment after 200-Hz conditioning in mut_{WR} calyx synapses indicates that the C_2B pathway operates also in the absence of the Ca^{2+}-CaM pathway and partially compensates for its loss.

Because of the similarity of the functional deficits between mut_{DN} versus mut_{WR} synapses and the spatial proximity of the C_2B domain and the Ca^{2+}-CaM binding site, we tested whether blocked Ca^{2+} binding to the C_2B domain perturbs Ca^{2+}-CaM binding. Co-immunoprecipitation experiments showed unaltered Ca^{2+}-CaM binding of the C_2BDN mutant Munc13-1 (Figure 5B).

These data indicate that the Munc13-1 regulation via the C_2B domain is likely downstream of or independent from the regulation by Ca^{2+}-CaM and that Ca^{2+} binding to the C_2B domain is not a pre-requisite for Ca^{2+}-CaM binding. Whether these pathways operate independently or synergistically to regulate Munc13-1 function and SVR remains to be studied.

The Munc13-1 C_2BKW mutation accelerates eEPSC recovery following conditioning trains

We next analyzed SVR in C_2BKW synapses. The recovery time course in mut_{KW} synapses was profoundly accelerated as compared to WT_{kw} (Figure 6A) and well described by a single fast exponential time constant. Little differences in fractional recovery were observed between mut_{KW} and WT_{KW} synapses for the two shortest recovery intervals (125 and 250 ms), while already 2 s after conditioning, $eEPSC_{test}$ had either nearly completely (100 Hz) or completely (200 Hz) recovered in mut_{KW} synapses (Figures 6A2 and 6A3; Table S1). For 200-Hz conditioning, we noticed average amplitudes of $eEPSC_{test}$ slightly larger than those of $eEPSC_1$.

To exclude that accelerated $eEPSC_{test}$ recovery in mut_{KW} synapses reflects $\overline{p}$ augmentation rather than faster SVR, we recorded $eEPSC_{test}$ pairs to monitor *PPRs*. If $\overline{p}$ were indeed higher in mut_{KW} synapses at 2- or 4-s recovery intervals as compared to 16 s, we would expect different *PPRs* at these time points. *PPRs*

Figure 4. Total number of releasable SVs and average initial release probability in C_2BDN and C_2BKW calyx synapses

Estimates for the readily releasable SV pool were derived from high-frequency eEPSC trains (*FRP*; A and B) and presynaptic ΔC_m measurements (*FRP* + *SRP*; C and D).

(A) Mean cumulative eEPSC amplitudes measured in response to stimulation with 50-, 100-, and 200-Hz trains (35 APs) in C_2BDN (A1) and C_2BKW (A2) synapses of WT (left) and mut (right) littermates. Solid, broken, and dotted lines represent regression lines correcting for ongoing SVR for 200-, 100-, and 50-Hz trains, respectively, assuming a constant average recruitment $\bar{r}_{+} \times q$. Intersections of these lines with the abscissa represent apparent pool size estimates (*FRP′*).

(B) $1/FRP'$ and apparent average release probability for $eEPSC_1$ ($\overline{p}' = eEPSC_1/FRP'$, insets) plotted versus inter-stimulus interval for C_2BDN (B1) and C_2BKW (B2) calyx synapses. Gray and colored symbols represent mean values for WT and mut synapses, respectively. Solid lines represent linear regressions to the scatterplots. Intersections of the line fits with the abscissa (at *ISI* = 0 ms) represent corrected estimates for $1/FRP_{corr}$ and $\overline{p}_{corr}$.

(C) Traces of presynaptic $I_{Ca(V)}$ (left) and ΔC_m (right) elicited by step depolarizations of 1, 2, 5, 10, and 20 ms duration in voltage-clamped C_2BDN (C1) and C_2BKW (C2) calyx terminals of WT (top row) and mut (bottom row) littermates.

(D) Average ΔC_m values plotted versus step duration for C_2BDN (D1) and C_2BKW (D2) calyx terminals. The numbers of SVs, obtained by assuming a single SV capacitance of ~80 aF (Sakaba, 2006), are shown on the right axis.

(E) Relationships between stimulus frequency f_{stim} and average replenishment rate constant $\overline{k}_{+}$ for WT C_2BDN (filled circles) and WT C_2BKW (empty circles) calyx synapses (E1) and for mut C_2BDN (red) and mut C_2BKW (blue) calyx synapses (E2). As the two WT datasets are nearly indistinguishable, the gray symbols in E2 represent their average. Axis and tick mark labels in the graphs shown in the bottom rows of (A), (B), and (D) also apply to the graphs of the top rows of the respective panels but were omitted for clarity.

Data depict mean ± SEM; n values and statistical significance are summarized in Table S1. See also Figures S3 and S6.

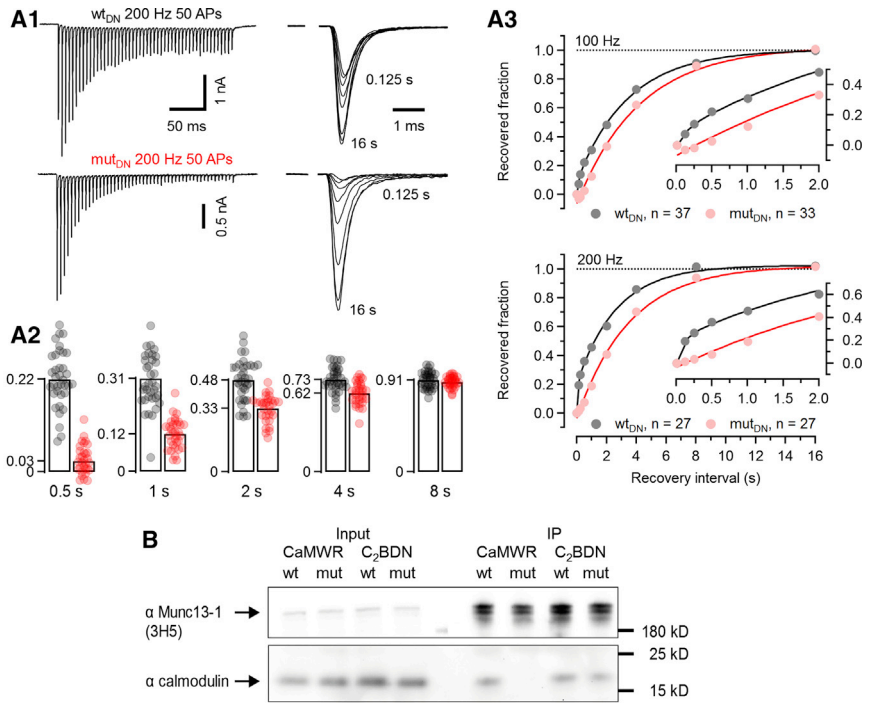

Figure 5. C_2BDN synapses recover more slowly from synaptic depression after high-frequency conditioning

(A) STD was induced by 100-Hz (25 APs) or 200-Hz (50 APs) conditioning stimulation, and recovery of eEPSC amplitudes was assayed at various intervals ($eEPSC_{test}$ measured after 0.125, 0.25, 0.5, 1, 2, 4, 8, and 16 s) in C_2BDN synapses. (A1) Traces of 200-Hz trains (left column) and $eEPSC_{test}$ recorded at different individual recovery intervals (right column) for a WT_{DN} (top row) and a mut_{DN} (bottom row) calyx synapse. (A2) Bar graphs and scatter dot plots representing average values and individual synapses, respectively, of the recovered fraction of the $eEPSC_{test}$ amplitude for different recovery intervals. (A3) Average time course of eEPSC recovery from synaptic depression after 100-Hz (top) or 200-Hz (bottom) conditioning trains. Insets show the early recovery of $eEPSC_{test}$ amplitudes at an expanded timescale.

(B) Co-immunoprecipitation of Munc13-1 from crude synaptosomal fractions obtained from brains of C_2BDN and CaMWR mutant mice and corresponding WT littermates.

Data depict mean ± SEM; n values and statistical significance are summarized in Table S1. See also Figures S4–S6.

measured after 2- and 4-s recovery in mut_{KW} synapses were indistinguishable from those measured at 16 s in either mut_{KW} or WT_{KW} synapses, indicating similar $\bar{p}$ values at the respective recovery intervals (Figure 6B).

To further corroborate that faster recovery from STD in mut_{KW} synapses primarily stems from faster SVR, we assayed SV pool recovery directly by presynaptic ΔC_m recordings. The duration of presynaptic depolarizations was limited to 3 ms to limit fusion of slowly releasing SVs (Sakaba and Neher, 2001b). Recovery of ΔC_m was noticeably faster in mut_{KW} as compared to WT_{KW} calyx terminals (Figure 6C) and resembled the accelerated eEPSC recovery time course (Figure 6A).

We then tested whether accelerated recovery from STD in mut_{KW} synapses is only observed after high-frequency conditioning (100 and 200 Hz), leading to substantial temporal summation of AP-evoked presynaptic global $[Ca^{2+}]_i$ transients, or if it is also seen following low-frequency conditioning (10 and 20 Hz), during which individual AP-evoked $[Ca^{2+}]_i$ transients decay nearly completely (Müller et al., 2007 and see below). We found that lowering the number of conditioning stimuli together with their frequency considerably slows down eEPSC recovery (Figures S4A3 and S4B3). However, at any tested conditioning frequency, recovery from STD occurred faster in mut_{KW} as compared to WT_{KW} synapses (Figures 6A and S4C). A detailed analysis of the relationship between the estimated steady-state $\bar{k}_+$ during stimulus trains versus the fractional recovery at different intervals after a conditioning train for all three mutants at the level of individual synapses is presented in Figure S6.

These data show that, in the Munc13-1 C_2BKW mutant with enhanced Ca^{2+}-dependent phospholipid binding to the C_2B domain, SVR is accelerated after low- and high-frequency conditioning. Faster recovery of eEPSC amplitudes is not driven by an elevated release probability during the recovery period.

Augmenting presynaptic AP-evoked Ca^{2+} influx does not mimic the acceleration of SV recruitment caused by the C_2BKW mutation

The accelerated eEPSC recovery after high-frequency trains in mut_{KW} synapses is reminiscent of faster recovery from STD upon increased presynaptic Ca^{2+} influx in calyx synapses (Wang and Kaczmarek, 1998). We tested whether widening of calyceal APs by TEA, thus augmenting presynaptic Ca^{2+} influx, induces fast SVR in WT synapses similar to that seen in mutant C_2BKW synapses. Bath application of TEA in the presence of kyn enhanced $eEPSC_1$ >4-fold and strongly increased STD (Figure 6D1). Unexpectedly, though, we observed only a moderate acceleration of the eEPSC recovery time course (Figure 6D2).

To resolve the apparent discrepancy between our results and those of Wang and Kaczmarek (1998), we repeated our experiments in the presence of the high-affinity, slowly dissociating AMPAR antagonist NBQX instead of the low-affinity, fast-dissociating antagonist kyn. With 100 nM NBQX, adequate voltage-clamp is ensured by reducing eEPSCs to a size comparable to that observed with kyn in the bath, while eEPSCs are still subject to AMPAR saturation and desensitization (Wadiche and Jahr, 2001). Augmentation of eEPSCs following TEA application was considerably smaller (<3-fold; Figures S7A and S7B) in the presence of NBQX instead of kyn, indicative of postsynaptic AMPAR saturation (Taschenberger et al., 2002, their Figure 8). eEPSC recovery after conditioning 100- or 200-Hz trains was profoundly accelerated by TEA (Figure S7A2), while $eEPSC_{ss}$ was similar to control conditions (100-Hz conditioning) or even reduced

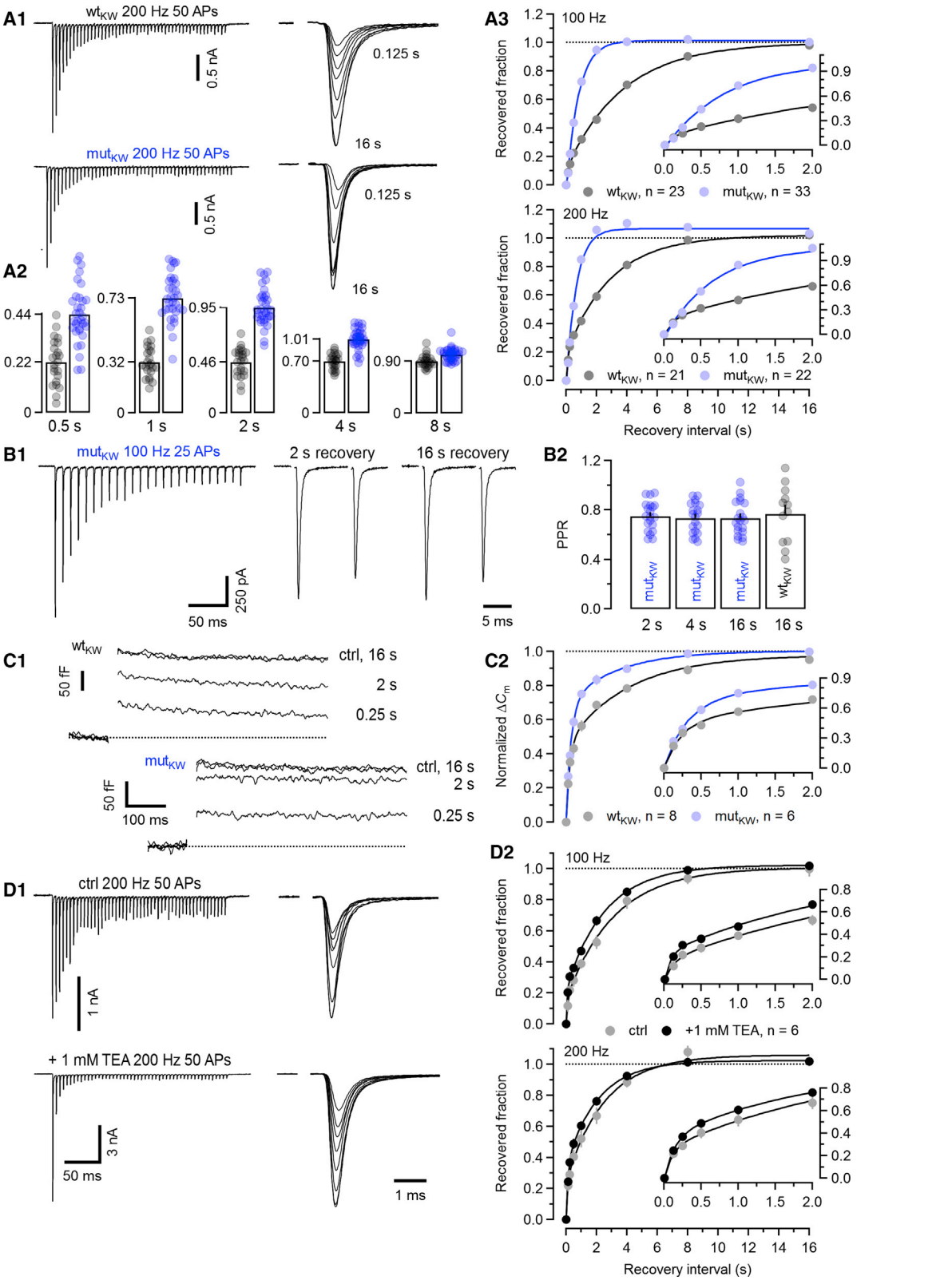

(legend on next page)

(200-Hz conditioning; Figure S7A1), which is unexpected if SVR during steady state was strongly enhanced by TEA.

These data show that, under conditions that limit AMPAR saturation and desensitization, SVR acceleration by enhanced Ca^{2+} influx is substantially smaller than that seen in mut_{KW} synapses. We conclude that the C_2BKW-mutation-induced SVR enhancement is not mimicked solely by augmenting AP-evoked Ca^{2+} influx. Rather, it reflects a combined regulatory effect of Ca^{2+} and phospholipid binding on Munc13-1 activity, whose magnitude is unique.

AP-evoked $[Ca^{2+}]_i$ transients in calyx terminals are unaltered in C_2BDN and C_2BKW synapses

To rule out that changes in the dynamics of presynaptic $[Ca^{2+}]_i$ due to differences in Ca^{2+} buffering or clearance contribute to the altered eEPSC recovery kinetics in mut_{DN} and mut_{KW} synapses, we measured $[Ca^{2+}]_i$ transients in response to afferent-fiber stimulation in nearly unperturbed calyx terminals preloaded with the low-affinity Ca^{2+} indicator dye Cal520FF (~1 min; Figures 7A and 7B; Habets and Borst, 2005; Müller et al., 2007). Maximum $[Ca^{2+}]_i$ amplitudes during trains were on average ~7 (100 Hz) and 16–18 (200 Hz) times larger than those of single AP-evoked transients. As described (Müller et al., 2007), calyceal $[Ca^{2+}]_i$ transients decayed bi-exponentially with a slow τ in the hundreds of millisecond range, which became more prominent after repetitive AP firing. When superimposing $[Ca^{2+}]_i$ transients recorded in either mut or WT C_2BDN or C_2BKW terminals, their waveforms were indistinguishable (Figure 7C; Table S1).

Having established the average time course of global $[Ca^{2+}]_i$ transients induced by conditioning trains, we modeled the recovery from SV pool depletion in C_2BDN and C_2BKW synapses by considering a SVR process that obeys a first-order rate law (Hosoi et al., 2007) and by using the previously established relationship between f_{stim} and $\overline{k}_+$ (Figure 4E). We assumed that the latter also predicts the relationship between global $[Ca^{2+}]_i$ and $\overline{k}_+$, i.e., we postulated a linear relationship between f_{stim} and $[Ca^{2+}]_i$ at steady state. Numerical simulations (Figure 7D) capture the essential features of the C_2B-mutation-induced changes, indicating that the altered dynamic regulation of $\overline{k}_+$ allows us to predict changes in pool recovery time course that correspond to the experimental observations. On the other hand, the simulations do not reproduce the initial "negative" or the "overshooting" eEPSC recovery observed in mut_{DN} (Figure 5A3) and mut_{KW} (Figure 6A3) synapses, respectively, indicating that a more detailed model, covering the heterogeneity in p as well as changes in p during and after conditioning stimulation, is required to more faithfully reconstruct the eEPSC recovery time course.

The data above—along with the facts that $I_{Ca(V)}$ amplitudes, VGCC gating kinetics, and $I_{Ca(V)}$ facilitation time course during AP-like stimulus trains are unaltered—indicate that changes in presynaptic Ca^{2+} signaling do not contribute to altered SVR kinetics in C_2BDN and C_2BKW synapses. Numerical simulations based on measured parameters predict the major features of C2B-mutation-induced changes in the pool recovery time course.

Temporal precision of information processing at calyx synapses deteriorates in the absence of fast SV recruitment

Calyx of Held synapses operate with high temporal precision, even at high transmission rates, leading to reliable AP firing of MNTB PNs (Guinan and Li, 1990; Kopp-Scheinpflug et al., 2008; Lorteije et al., 2009). In addition to other features (Borst and Soria van Hoeve, 2012; Schneggenburger and Forsythe, 2006; von Gersdorff and Borst, 2002), an activity-dependent SVR upregulation may critically contribute to sustained and temporally precise transmission. We thus tested whether the Munc13-1 mutations affect information processing at calyx synapses by analyzing postsynaptic AP timing following afferent fiber stimulation.

Recordings from MNTB PNs in cell-attached configuration represent a minimally invasive form of monitoring postsynaptic Na^+ spikes with high signal-to-noise ratio, allowing analyses of AP timing with microsecond precision (Figures 8A and 8B; Lorteije et al., 2009). Extracellularly recorded APs measured during the recovery period following conditioning stimulation are shown superimposed in Figures 8A2 and 8B2. In WT synapses, a clear right shift in the AP timing relative to stimulus onset is seen for short recovery intervals, showing that small evoked excitatory postsynaptic potentials (eEPSPs), generated while the *FRP* is

Figure 6. C_2BKW synapses recover faster from synaptic depression after high-frequency conditioning

(A) Similar experiments as in Figure 5A but in C_2BKW synapses. (A1) Traces of 200-Hz trains (left column) and $eEPSC_{test}$ recorded at different recovery intervals (right column) for a WT_{KW} (top row) and a mut_{KW} (bottom row) calyx synapse. (A2) Bar graphs and scatter dot plots representing average values and individual synapses, respectively, of the recovered fraction of $eEPSC_{test}$ amplitude for different recovery intervals. (A3) Average time course of eEPSC recovery from synaptic depression after 100-Hz (top) or 200-Hz (bottom) conditioning trains.

(B) Comparison of *PPR*s during the recovery time course in C_2BKW synapses. (B1) Traces of $eEPSC_{test}$ pairs (10 ms *ISI*) following 100-Hz conditioning trains (left) recorded at recovery intervals of either 2 s (middle) or 16 s (right) in a mut_{KW} synapse. (B2) Bar graphs and scatter dot plots representing average values and individual synapses, respectively, of *PPR*s measured after 2, 4, and 16 s recovery in mut_{KW} synapses (left bars, blue symbols) in comparison to 16 s recovery in WT_{KW} synapses (right bar, gray symbols).

(C) Recovery from SV pool depletion assayed by presynaptic ΔC_m recordings. SV pool depletion was induced by applying step depolarizations of 3 ms duration from $V_h = -80$ mV to 0 mV, and recovery was monitored at intervals ranging from 0.125 s to 16 s after the end of the depolarization. (C1) Sample ΔC_m traces for control and 0.25-s, 2-s, and 16-s recovery intervals recorded in a WT_{KW} (top) and a mut_{KW} (bottom) calyx terminal are shown. For clarity, ΔC_m traces in this panel were low-pass filtered with a moving average kernel of width 7. (C2) Average recovery time course of ΔC_m measured in WT_{KW} (gray) and a mut_{KW} (blue) calyx synapse.

(D) (D1) Similar experiment as illustrated in (A) but recorded in a WT synapse in the absence (top row) and presence (bottom row) of 1 mM TEA to broaden presynaptic APs and enhance presynaptic Ca^{2+} influx. All recordings were obtained in the presence of 1 mM kyn. (D2) Average time course of eEPSC recovery after 100- (top) or 200-Hz (bottom) conditioning trains recorded in the absence (gray symbols) or presence (black symbols) of 1 mM TEA. Enhancing presynaptic Ca^{2+} influx accelerated recovery of $eEPSC_{test}$ but to a much lower extent than in C_2BKW synapses (compare A3 and D2).

Data depict mean ± SEM; n values and statistical significance are summarized in Table S1. See also Figures S4, S6, and S7.

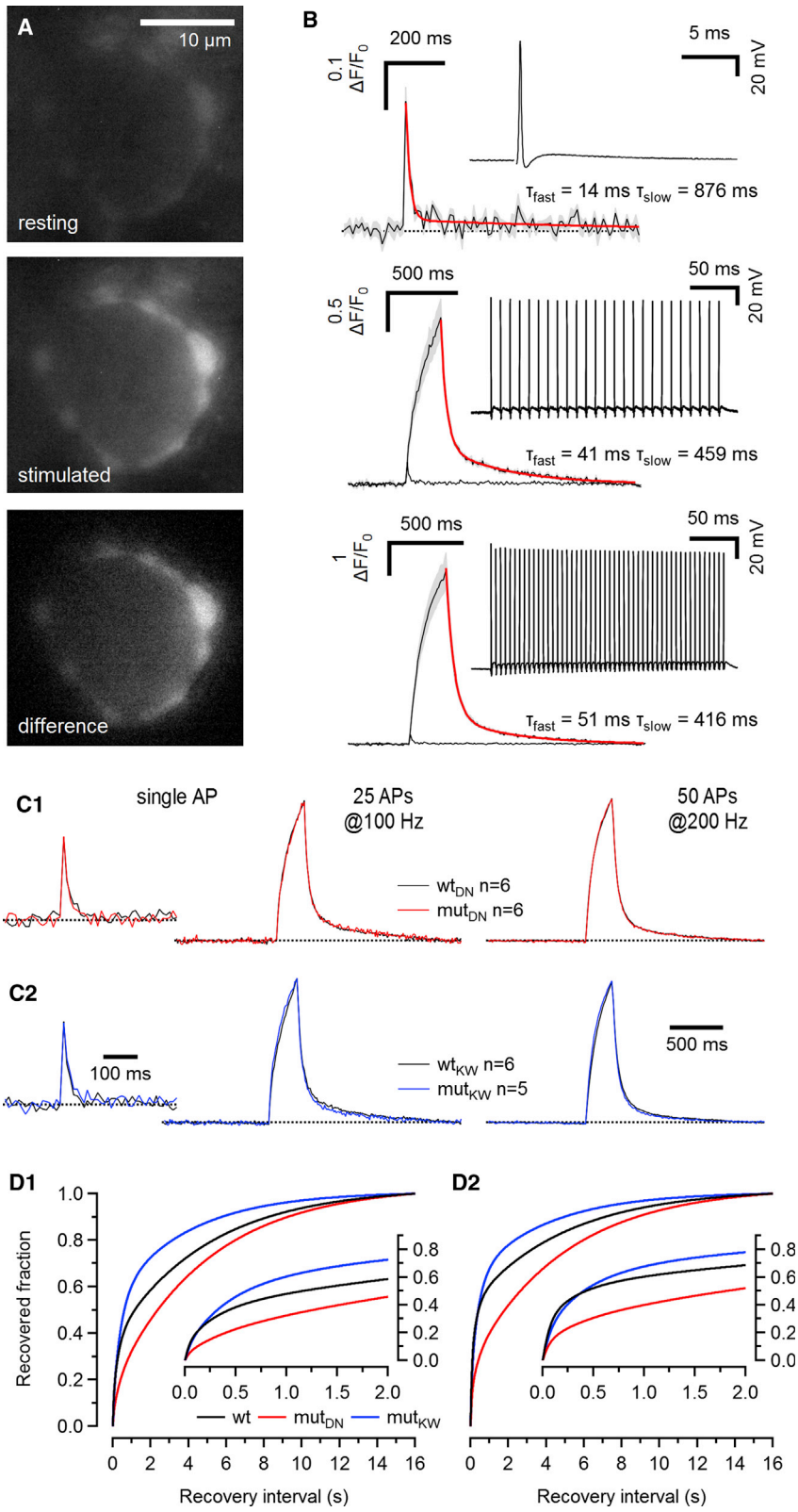

Figure 7. AP-evoked global volume-averaged $[Ca^{2+}]_i$ transients in calyx terminals

(A) Fluorescence images of a calyx terminal preloaded with the low-affinity Ca^{2+} indicator dye Cal520FF (K_D = 9.8 µM) during a brief whole-cell episode (~1 min; pipette concentration 400 µM; final cytosolic concentration ~200 µM) at rest (top) and during 200-Hz stimulation (50 APs, center). The difference image is shown in the bottom panel.

(B) Presynaptic $[Ca^{2+}]_i$ transients ($\Delta F/F_0$) elicited by a single AP (top) or trains of 25 (100 Hz, center) or 50 APs (200 Hz, bottom), corresponding to stimulus trains used for Figures 5A, 6A, and 6D. Each trace represents the average of 6 (single AP) or 4 (AP trains) repetitions, and the gray areas represent ±SEM. AP discharge pattern recorded in response to afferent fiber stimulation under current-clamp conditions during the preloading period is illustrated in the top right insets. Red traces represent double-exponential fits to the decay of the $[Ca^{2+}]_i$ transients. Fast- and slow-decay time constants are given next to the $[Ca^{2+}]_i$ transients. The single AP response is shown superimposed to the train responses in the center and bottom panels for comparison.

(C) Normalized average presynaptic $[Ca^{2+}]_i$ transients recorded in WT (back) and mut (red and blue) C_2BDN (C1) and C_2BKW (C2) terminals in response to a single AP (left), a 100-Hz AP train (25 APs, center), or a 200-Hz AP train (50 APs, right).

(D) Numerical simulations of SV pool recovery after 100-Hz (left) and 200-Hz (right) trains assuming first-order kinetics and a $[Ca^{2+}]_i$-dependent $\overline{k}_+$. For simplicity, we approximated the relationship between $\overline{k}_+$ and $[Ca^{2+}]_i$ by assuming a linear relationship between f_{stim} and $[Ca^{2+}]_i$ at steady state. The decay of $\overline{k}_+$ immediately after conditioning trains (corresponding to t = 0 s in D) was modeled with a double-exponential function using decay time constants established by fitting the average $[Ca^{2+}]_i$ transients shown in (C).

largely depleted, mostly trigger postsynaptic APs with longer latencies. Strikingly, mut_{DN} synapses, which lack the fast component of eEPSC recovery, tended to show even longer latencies between stimulus and postsynaptic spike for short recovery intervals.

Temporal jitter and timing of postsynaptic APs was further analyzed in whole-cell configuration to obtain stable long-term recordings and to collect more repetitions of a given protocol (Figures 8C and 8D). In rare cases, individual aberrant postsynaptic APs were triggered during conditioning, presumably by asynchronous release events generating supra-threshold eEPSPs, so that the number of postsynaptic APs exceeded the number of stimuli in some trials (Figure 8C1). As in cell-attached recordings, we observed longer AP latencies at short recovery intervals in mut_{DN} as compared to WT_{DN} synapses. In addition, we found that the temporal jitter increased (Figure 8D2). Conversely, mut_{KW} synapses showed improved temporal precision as compared to WT synapses, so that AP latencies were shorter and spike latency jitter was reduced for a range of short recovery intervals (0.5–4 s; Figure 8D3). Figures 8E and 8F plot the average increase in spike latencies relative to those measured for the longest recovery interval (16 s) and the mean of the standard deviation of the timing of AP peaks as a measure of spike timing variability. In both WT and mut_{KW} synapses, AP latencies were ~200 μs longer for the shortest recovery interval (0.125 s) than those after 16 s recovery. In mut_{DN} synapses, the spike latency increase for short recovery intervals was nearly twice as large and remained larger for all but the 4-s and 8-s intervals. In mut_{KW} synapses, on the other hand, AP latencies declined much faster with increasing recovery intervals. For 2–16 s recovery, no differences in spike timing were measurable, consistent with the fact that, for recovery intervals, ≥2 s eEPSCs had nearly fully recovered after conditioning 100-Hz stimulation (Figure 6A3). A similar picture emerged for the temporal jitter of AP latencies. For intervals ≤1 s, the jitter was larger in mut_{DN} but generally smaller in mut_{KW} synapses as compared to WT synapses (Figure 8F).

These data show that the modulation of SVR speed mediated by Ca^{2+}-phospholipid binding to the Munc13-1 C_2B domain influences synapse fidelity. This phenomenon is expected to alter synaptic computation at the level of single synapses and circuits.

Faster rebound from synaptic depression at hippocampal synapses upon acceleration of SV recruitment

To show that the rate of Munc13-1-dependent SVR also determines STP at synapses that are less prone to rapid SV pool exhaustion at their typical firing rates (Mizuseki and Buzsáki, 2013), we analyzed transmission at P16–P21 hippocampal Schaffer collateral/commissural synapses with CA1 neurons (SC/C-CA1), focusing on C_2BKW mice (Figure 8G). We conditioned SC/C-CA1 synapses with 10-Hz trains. This stimulus frequency was chosen to limit the contribution of synaptic augmentation during recovery from STD and to avoid post-tetanic potentiation. We observed a slight initial paired-pulse facilitation (1.09 ± 0.05 and 1.05 ± 0.03 in WT_{KW} and mut_{KW} synapses, respectively), followed by depression, during which steady-state eEPSC amplitudes were reduced to ~55% as compared to the maximum eEPSC size measured during trains, indicating an *RRP* depletion of ≥45%. Following conditioning, eEPSCs recovered within 5–10 s to an amplitude that was ~20% larger than $eEPSC_1$ of the conditioning train (Garcia-Perez and Wesseling, 2008). While levels and decay time constants (~9 s) of synaptic augmentation were similar in WT_{KW} and mut_{KW} synapses, the rebound from STD was accelerated in mut_{KW} synapses, particularly at 1- to 2-s recovery intervals (Figures 8H1 and 8H2). To corroborate a more complete SV pool recovery after 2 s recovery from STD, we approximated in a subset of synapses the relative *RRP* occupancy by estimating the ratio of $RRP_{2\ s}/RRP_{16\ s}$, assuming that pool recovery has completed after 16 s recovery. The corresponding ratio was larger in mut_{KW} (96% ± 3%) as compared to WT_{KW} (82% ± 5%) SC/C-CA1 synapses (Figure 8H3).

These data show that SVR acceleration by Munc13-1 affects short-term plasticity also at strongly augmenting synapses, indicating a fascinating interplay between different short-term plastic processes that shapes the distinct features of different synapse types.

DISCUSSION

Munc13s are essential SV priming proteins, in whose absence no fusion-ready SVs are formed and synaptic transmission ceases (Sigler et al., 2017; Varoqueaux et al., 2002). Studies with cultured neurons showed that Munc13 activity can be regulated by Ca^{2+}-CaM binding to an amphipathic helix motif (Junge et al., 2004; Lipstein et al., 2012), by DAG binding to a central C_1 domain (Betz et al., 1998; Rhee et al., 2002), and by Ca^{2+}-phospholipid binding to an adjacent C_2B domain (Shin et al., 2010). What has remained unknown is how these regulatory processes affect synapse function downstream of SV priming and whether they are used purposively in intact networks to shape computational synapse properties. We show here that Munc13-1 is regulated by convergent Ca^{2+}- and phospholipid-dependent signaling to adjust SV priming rates, enable sustained transmission, and ensure temporal fidelity of synaptic signaling in intact circuits.

To assess the role of Ca^{2+}- and phospholipid-dependent regulation of Munc13-1 function in intact circuits, we generated KI mice that express Munc13-1 variants with abolished (Munc13-$1^{D705/711N}$) or increased Ca^{2+}-dependent phospholipid binding to the C_2B domain (Munc13-1^{K706W}; Shin et al., 2010) and characterized functional consequences in the calyx of Held synapse. Our data demonstrate an activity-dependent activation of Munc13-1 via its C_2B domain. In the absence of Ca^{2+}-regulated phospholipid binding to the Munc13-1 C_2B domain, fast SVR during and immediately after high-frequency AP trains is strongly attenuated, resulting in reduced transmitter release and perturbed temporal precision of synaptic transmission following bursts of activity. Conversely, increasing the Ca^{2+}-dependent PIP_2 affinity of the Munc13-1 C_2B domain enhances SVR, augments synaptic strength during and following presynaptic AP trains, and improves temporal precision of transmission. The fact that the mutation-induced bidirectional manipulation of Ca^{2+}-phospholipid binding to the Munc13-1 C_2B domain leads to corresponding bidirectional changes in SVR rates demonstrates the existence of a Ca^{2+}-phospholipid-sensing regulatory process in SV priming within intact

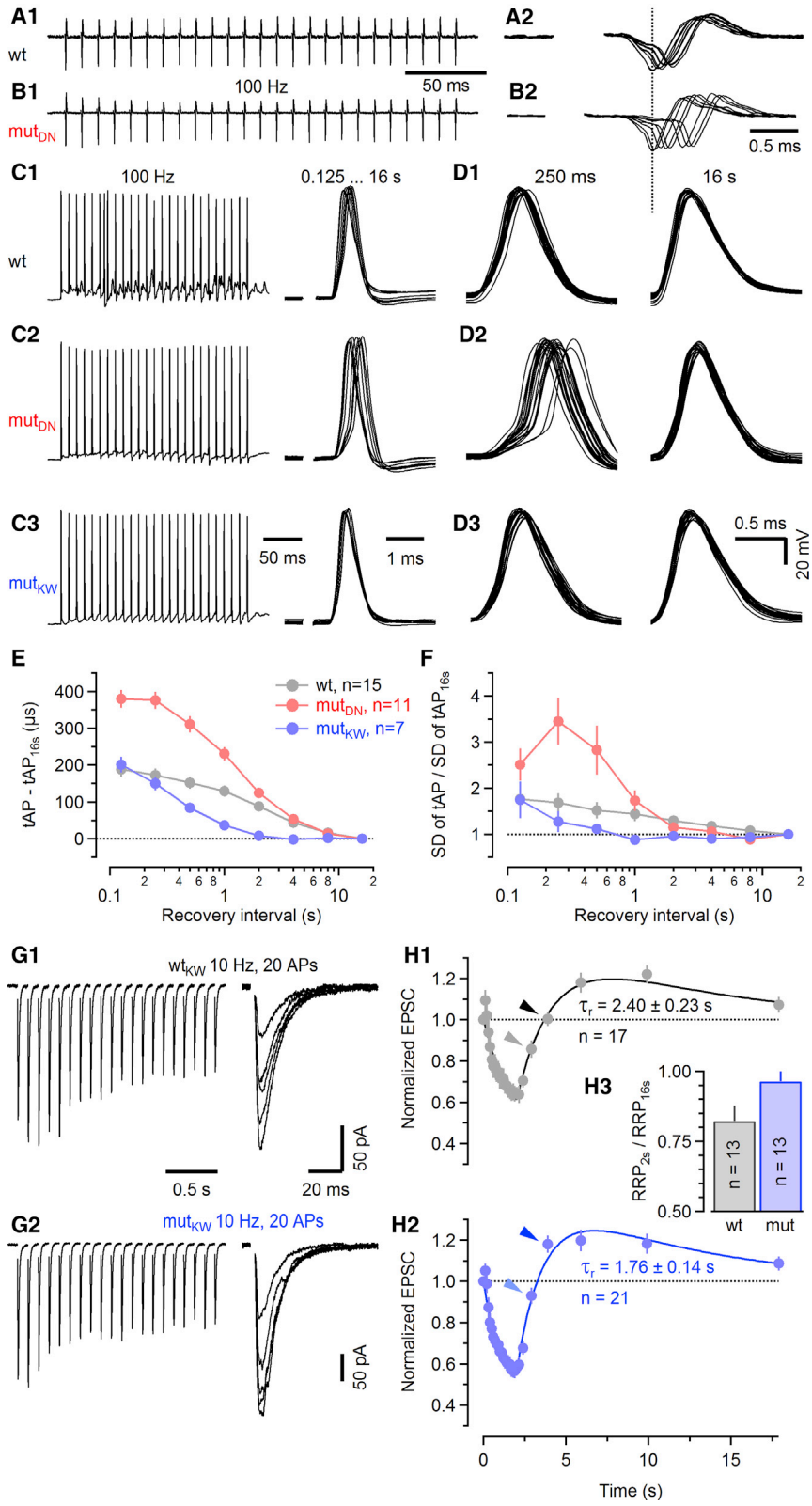

Figure 8. Munc13-1-dependent SV priming affects the AP timing in MNTB principal neurons during recovery from synaptic depression and accelerates the rebound from synaptic depression at hippocampal Schaffer collateral-CA1 synapses

(A–F) Recordings in brainstem slices obtained in the absence of kyn.

(A and B) Cell-attached recordings of postsynaptic APs triggered in MNTB PNs in response to afferent fiber stimulation during a 100-Hz (25 stimuli) train (A1 and B1) and at various recovery intervals (A2 and B2) in a WT_{DN} (A) and a mut_{DN} (B) synapse. All eight recovery intervals (0.125, 0.25, 0.5, 1, 2, 4, 8, and 16 s) were tested in a single sweep to shorten the duration of the recording protocol. APs recorded during recovery from synaptic depression are shown superimposed after alignment to the stimulus onset. Traces shown in B2 are temporally slightly offset to align the negative peak of the AP recorded after 16 s recovery (dotted line) in the mut_{DN} with that of the corresponding WT_{DN} synapse to facilitate latency fluctuation comparison.

(C) Similar experiment as in (A) and (B), but postsynaptic APs were recorded intracellularly under current-clamp conditions during the 100-Hz trains (left) and for various test intervals (superimposed, right).

(D) Latency fluctuations for APs recorded 0.25 s (left) and 16 s (right) after conditioning 100-Hz trains. 21 consecutive trials are shown superimposed.

(E and F) Summary data for latencies of intracellularly recorded postsynaptic APs (E) and fluctuations of AP timing (F) plotted versus recovery interval. Data from WT synapses of both KI lines were similar and therefore pooled. AP latencies are expressed relative to the timing of the AP peak for 16-s recovery interval ($tAP_{16\ s}$) (E). Changes in latency fluctuations are expressed as the ratio of the SD of tAP relative to the SD of $tAP_{16\ s}$ (F).

(G and H) Recordings in P16–P21 hippocampal slices, obtained using 2 mM Ca^{2+} and 1 mM Mg^{2+} in the bath solution and in the absence of kyn.

(G) Recovery from STD induced by 10-Hz stimulus trains (20 APs) at hippocampal SC/C-CA1 synapses of a C_2B WT_{KW} (G1) and a C_2B mut_{KW} (G2) mouse (left panels). Recovery was probed by recording a single $eEPSC_{test}$ evoked at increasingly longer recovery intervals (0.125, 0.25, 0.5, 1, 2, 4, 8, and 16 s), which are shown superimposed (right panels).

(H) Average time course of eEPSC amplitudes during conditioning 10-Hz stimulation and the subsequent recovery from STD, obtained from WT_{KW} (H1) and mut_{KW} (H2) SC/C-CA1 synapses. At least three trials were averaged for each synapse tested. Smooth traces represent a model of synaptic plasticity fitted to the data. The model consisted of SV pool depletion and a stimulus-induced augmentation of the release probability, which slowly decayed in the absence of AP firing. Estimated SV pool recovery time constants τ_r were 2.40 s (WT_{KW}) and 1.76 s (mut_{KW}). Assuming that pool recovery has completed after 16 s, the relative pool occupancy at 2 s recovery was estimated as the ratio of $RRP_{2\ s}/RRP_{16\ s}$ for a subset of WT_{KW} and mut_{KW} synapses (H3).

Data depict mean ± SEM.

circuits and identifies Munc13-1 as its major target. We propose that Munc13-1 integrates Ca^{2+} and PIP_2 signaling to tune SVR speed according to the requirements imposed on the release machinery. We demonstrate that this regulatory process is relevant in calyx of Held and Schaffer collateral/commissural-CA1 synapses. Given that Munc13-1 is expressed in essentially all neurons of the brain (Augustin et al., 1999a), this regulatory principle is likely to operate in many brain circuits to control information processing.

The Munc13 C_2B domain

Five aspartic acid residues of the Munc13 C_2B domain coordinate two Ca^{2+} ions (Shin et al., 2010). Binding assays with the isolated C_2B domain indicate an apparent Ca^{2+} EC_{50} of 5.5 μM to promote phospholipid binding. Such high $[Ca^{2+}]_i$ is likely only reached near open VGCCs (Eggermann et al., 2011; Neher and Sakaba, 2008) or during high-frequency AP firing (Korogod et al., 2005; Lin et al., 2017). Our findings, showing that Ca^{2+}-dependent phospholipid binding to the C_2B domain promotes SVR, imply that the C_2B domain of Munc13s "sees" high $[Ca^{2+}]_i$ levels during AP firing.

The lipid binding properties of the Munc13-1 C_2B are rather unique, with PIP and PIP_2 binding preferentially and equally well. This may allow the domain to respond to subtle temporal and spatial changes in phosphoinositide (PI) second messenger levels, which occur during ongoing presynaptic activity, e.g., via Ca^{2+}-dependent regulation of phospholipases or PI kinases/phosphatases or upon activation of cell-surface receptors (Brown and Sihra, 2008). These considerations, and the fact that Munc13-1 acts as an AZ organizer (Sakamoto et al., 2018), lead to the notion of a dynamic interplay between the lipid and protein composition of SV fusion sites that is regulated by synaptic activity.

While the *RRP* is completely eliminated upon Munc13 loss (Siksou et al., 2009; Varoqueaux et al., 2002), several mutations of Munc13-1 regulatory domains reduce *RRP* size. This was observed in KI neurons expressing a DAG-insensitive Munc13-1 (Rhee et al., 2002) and subsequently with C_2A and C_2C deletion mutant Munc13-1 variants. The latter finding led to the notion that Munc13-1 may not only regulate SNARE complexes but also bridge SV and AZ plasma membranes, involving the C_1-C_2B tandem (Liu et al., 2016; Quade et al., 2019). The present study did not yield evidence for *RRP* changes upon elimination or enhancement of C_2B-lipid interactions, indicating that the C_2B mutations we introduced do not interfere with any membrane bridging function.

Certain Munc13 C2B mutations change presynaptic $[Ca^{2+}]_i$ transients in cultured neurons, presumably via VGCC modulation (Calloway et al., 2015). We observed no defects in calyceal $I_{Ca(V)}$ of C_2BDN and C_2BKW mutants. Likewise, AP-evoked global $[Ca^{2+}]_i$ transients in dye-preloaded calyces were unaltered, indicating that the major spatial aspects of AZ organization and AP-evoked presynaptic Ca^{2+} influx are intact in mut_{DN} and mut_{KW} synapses.

Phospholipid-dependent regulation of SV priming and fusion

Phospholipids are presumed to regulate Ca^{2+}-dependent vesicle fusion in neurons and neuroendocrine cells. Many presynaptic proteins have lipid-binding domains (Pinheiro et al., 2016), and PIP_2 is a major component of the plasma membrane at release sites (Kabachinski et al., 2014; Milosevic et al., 2005; Walter et al., 2017). PIP_2 likely clusters syntaxin (Honigmann et al., 2013; van den Bogaart et al., 2011) and other AZ components (de Jong et al., 2018), acts as a regulator of synaptotagmin-driven SV fusion (van den Bogaart et al., 2012), and is involved in presynaptic clathrin-mediated endocytosis (Jung and Haucke, 2007), also in the calyx of Held (Eguchi et al., 2012).

A major challenge in studying phospholipid-dependent regulation of synaptic protein function is that the dynamic lipid composition at AZs is unknown and difficult to manipulate experimentally. Most relevant data were obtained with *in vitro* analyses of neuroendocrine cells, where vesicle fusion occurs over the entire plasma membrane, and by pharmacologically manipulating phospholipid composition. The time course of such manipulations is slow, and they often lack specificity. Fast-acting, light-activated lipid compounds exist, but their activation is difficult to restrict to AZs (Frank et al., 2016; Walter et al., 2017). To circumvent these challenges, we chose a genetic approach, i.e., the mutagenesis of a single lipid-sensor protein. Interfering with the Ca^{2+}-phospholipid-dependent regulation of Munc13-1 strongly affects SVR speed. As pharmacologically enhancing AP-evoked Ca^{2+} influx alone only moderately speeds up SVR, we propose that AZ lipid composition modulates Munc13 activity to regulate SVR.

Phospholipid-binding properties of C_2BKW resemble those of the synaptotagmin-1 C_2A domain, with preference for PIP_2 over PIP and largely unaltered Ca^{2+} sensitivity (Shin et al., 2010). In mut_{KW} synapses, initial synaptic strength, *PPR*, and the rate of eEPSC depression during the onset of high-frequency trains are unaltered, indicating that $\overline{p}$ is unchanged. However, for all but the three highest stimulus frequencies (50–200 Hz), we determined increased steady-state replenishment rate constants $\overline{k}_+$. Elevated PIP_2 affinity of the mutated Munc13-1 C_2BKW domain thus augments SVR. During high-frequency stimulation, the elevated PIP_2 affinity of the mutated C_2BKW domain may become less important because elevated $[Ca^{2+}]_i$ enhances phospholipid binding to the C_2B domain also in WT synapses. Indeed, for high-frequency stimulation, enhancing AP-evoked presynaptic Ca^{2+} influx pharmacologically only moderately speeds up eEPSC recovery, indicating that $\overline{k}_+$ during 100- and 200-Hz conditioning is close to maximum even in WT synapses.

The C_2BDN mutation perturbs Munc13-1 function by replacing two aspartic acid residues, abolishing Ca^{2+} binding (Shin et al., 2010). We observed higher initial synaptic strength in mut_{DN} synapses as compared to WT. This is likely caused by higher $\overline{p}$, as *PPR*s are lower in Munc13-1 C_2BDN synapses, and synaptic depression during high-frequency trains proceeds faster while *RRP* is unaffected. An explanation for this unexpected finding is that the C_2BDN variant shows significant membrane binding in the absence of Ca^{2+} (Shin et al., 2010), which may lead to increased Munc13-1 C_2BDN activity at resting $[Ca^{2+}]_i$.

The interplay of regulatory domains of Munc13s

Three Ca^{2+}- and second-messenger-sensitive regulatory domains allow Munc13s to respond to a wide range of $[Ca^{2+}]_i$ and lipid second messengers. Ca^{2+}-CaM binding to Munc13s occurs

at sub-micromolar $[Ca^{2+}]_i$ (Dimova et al., 2006; Zikich et al., 2008), while the C_2B domain requires 2–10 μM $[Ca^{2+}]_i$ (Shin et al., 2010). Thus, Ca^{2+}-CaM-dependent regulation of Munc13s can operate at lower $[Ca^{2+}]_i$ than C_2B domain activation. As Munc13-1 is localized at AZs near VGCCs, it is possible that the C_2B domain preferentially senses brief local $[Ca^{2+}]_i$ transients in addition to large global $[Ca^{2+}]_i$ changes during prolonged high-frequency firing, while the high Ca^{2+} affinity of the Ca^{2+}-CaM pathway may allow efficient sensing of longer lasting and lower global $[Ca^{2+}]_i$ transients. DAG binding to the C1 domain allows Munc13 activation at timescales that exceed the duration of $[Ca^{2+}]_i$ transients as its termination depends on enzymatic DAG removal. It is therefore likely that the regulatory domains of Munc13s operate in a successive, cooperative, and synergistic fashion rather than redundantly.

We previously examined functional effects of a point mutation (Munc13-1^{W464R}; mut_{WR}) that renders Munc13-1 Ca^{2+}-CaM insensitive (Lipstein et al., 2013). Mut_{WR} calyces show much slower SV pool recovery following long presynaptic depolarizations, but recovery of AP-evoked eEPSCs following STD is less perturbed. The latter finding led to the conclusion that additional, possibly more effective, molecular pathways for $[Ca^{2+}]_i$-dependent SVR regulation must exist (Lipstein et al., 2013). The present study identifies Ca^{2+}-dependent phospholipid binding to Munc13-1 as such a pathway. The loss of fast eEPSC recovery in mut_{DN} synapses demonstrates that it plays a major role in Ca^{2+}-dependent SVR. This mechanism likely operates in concert with Ca^{2+}-CaM and DAG binding to adjust presynaptic function on demand, stressing the notion of Munc13s as a regulatory hub in SV priming.

The function of the Munc13 C2B domain—consensus and discrepancies

Multiple previous studies focused on Munc13 C_2B function, establishing it as a Ca^{2+}-phospholipid binding domain that controls Munc13 priming function and thus dynamically regulates transmitter release (Kabachinski et al., 2014; Michelassi et al., 2017; Shin et al., 2010). Beyond this, Munc13 C_2B interactions with AZ scaffold proteins (Brockmann et al., 2020) and VGCCs (Calloway et al., 2015) were reported. Unfortunately, a direct comparison of previous studies with ours is complex as different paralogs, mutations, neuronal preparations, synapse types, or organisms were studied.

Nevertheless, at least three general commonalities emerge. First, effective and specific blockade of Ca^{2+}-phospholipid binding to Munc13 C_2B reduces SV priming activity and attenuates synaptic transmission, albeit to different degrees und under different stimulation conditions (Kabachinski et al., 2014; Michelassi et al., 2017; Shin et al., 2010). Second, certain mutations in the Ca^{2+}-phospholipid-binding pocket of Munc13 C_2B can cause increased transmitter release, likely due to an increase in Ca^{2+}-independent phospholipid binding (Kabachinski et al., 2014; Michelassi et al., 2017; Shin et al., 2010). Third, Ca^{2+}-phospholipid-dependent regulation via the C_2B domain can modulate the dynamics of synaptic transmission upon prolonged high-frequency stimulation (Shin et al., 2010; present study), with different consequences for short-term plasticity. The remaining differences in the context of these commonalities likely arise due to differences in the neuronal membrane lipid composition present in the various preparations and synapse types studied.

Equally important are the facets that distinguish the present findings from previously published ones. Most importantly, the conclusions drawn from our work versus that of Shin et al. (2010) differ fundamentally. Whereas Shin et al. (2010) did not report evidence for a regulation of SVR rate by Munc13 C2B, we provide clear evidence for such a regulation. Aspects of this discrepancy might be due to different experimental conditions. This notwithstanding, our findings demonstrate that the presynaptic process of dynamic SV priming must ultimately be studied in intact circuits as they appear *in vivo* to determine its exact molecular features and computational role in circuits.

Synaptic depression and recovery at the calyx of Held synapse

Several mechanisms, including pool depletion, negative feedback via presynaptic metabotropic receptors, and postsynaptic receptor desensitization, contribute to synaptic depression (Zucker and Regehr, 2002). Synaptic transmission at post-hearing onset calyx synapses shows only limited sensitivity to auto-inhibition via mGluRs (Renden et al., 2005) or AMPARs desensitization and saturation (Taschenberger et al., 2002). Because we recorded eEPSCs in the presence of 1 mM kyn, further attenuating possible postsynaptic effects, we assume pool depletion as the principal cause for synaptic depression in our experiments.

STD is determined by a balance of SV recruitment and consumption. Recovery from synaptic depression is slow ($\tau \approx 4$ s) at calyx synapses when measured after stimuli that do not strongly increase global $[Ca^{2+}]_i$ (Iwasaki and Takahashi, 2001; von Gersdorff et al., 1997). Considering $\overline{k}_+ = \frac{1}{4\,s} = 0.25\,s^{-1}$ and a total number of SV docking sites (N) that approximately equals the size of the *FRP* (1,000–2,000 SVs), the SVR rate would be limited to 250–500 SV/s. For 200-Hz trains and $q \sim 60$ pA (Chang et al., 2015), this equates to an $eEPSC_{ss}$ of only 75–150 pA (~8–17 pA for recordings in 1 mM kyn), which is much less than experimentally observed. In fact, we estimated a 16-times-higher $\overline{k}_+$ of $\sim 4\,s^{-1}$ to predict the observed steady-state release rates during 200-Hz trains. Our $\overline{k}_+$ estimate rests on the assumption that N is approximately equal to the *FRP* size, i.e., that the occupancy (p_{occ}) of docking sites in resting calyces is close to 100%. If p_{occ} were substantially lower (Malagon et al., 2020), we would need to postulate a larger N and, consequently, lower $\overline{k}_+$.

Assuming a strongly upregulated $\overline{k}_+$ during high-frequency conditioning, which then decays to its basal value after cessation of stimulation, we expect a biphasic eEPSC recovery time course. During low-frequency conditioning, $\overline{k}_+$ increases much less, which explains the absence of a fast component of eEPSC recovery. However, the mere existence of a biphasic eEPSC recovery alone is insufficient proof for a Ca^{2+} dependence of SVR (Hallermann et al., 2010), and for some synapses, experimental interference with either $[Ca^{2+}]_i$ or its sensor binding did not indicate a Ca^{2+} dependence of SVR (Miyano et al., 2019; Ritzau-Jost et al., 2018). Nevertheless, the findings that, in calyx synapses, eEPSC recovery is accelerated upon augmenting presynaptic Ca^{2+} influx (Wang and Kaczmarek, 1998) and sensitive to

manipulations that interfere with Ca^{2+} binding to CaM (Sakaba and Neher, 2001a), with Ca^{2+}-CaM binding to Munc13-1 (Lipstein et al., 2013), or with Ca^{2+}-phospholipid binding to Munc13-1 (present study) support the notion that the fast component of pool recovery is regulated by elevated $[Ca^{2+}]_i$.

For 200-Hz stimulation of WT synapses, we estimated a $\overline{k}_+$ of ~4 pools/s at steady state. Assuming a linear relationship between global $[Ca^{2+}]_i$ and SVR rate constant according to $\overline{k}_+ = k_{basal} + \alpha \times [Ca^{2+}]_i$, with $k_{basal} = 0.1\ s^{-1}$ and a slope factor α of ~1 pool/(μM × s) (Hosoi et al., 2007), this corresponds to $[Ca^{2+}]_i$ of ~3.9 μM. Such supra-micromolar global $[Ca^{2+}]_i$ values of ~1.4 μM and in the range of 3–10 μM were previously reported for voltage-clamped WT calyces stimulated with 200-Hz AP waveform trains (Lin et al., 2017) and for dye-preloaded WT calyces during prolonged 100-Hz firing (Korogod et al., 2005), respectively.

Munc13-1-controlled SV recruitment and information processing in single synapses and synaptic circuits

Our analyses of postsynaptic AP latency and jitter show that altered SVR can affect information transfer at calyx synapses. Consistent with the "failsafe" operation of calyx synapses (Guinan and Li, 1990; Lorteije et al., 2009), we never observed spike failures during or following AP trains. In comparison to WT, mut_{DN} synapses show longer AP latencies and reduced temporal precision of transmission following conditioning trains. In contrast, mut_{KW} synapses show improved temporal precision and shorter AP latencies. This demonstrates that the SVR speed determines postsynaptic AP timing after bouts of presynaptic activity. This may have only subtle functional consequences at the calyx of Held, particularly with faster SVR at physiological temperature (Kushmerick et al., 2006). However, profound effects on the reliability of postsynaptic firing are likely at the many less failsafe synapses in the brain or in scenarios where neurons summate multiple synaptic inputs for triggering AP firing. In the corresponding circuits, the dynamic regulation of Munc13-1 activity by Ca^{2+} and phospholipids is expected to have substantial effects on information processing.

Our experiments on SC/C-CA1 synapses show that an acceleration of SVR speed also affects STP at small hippocampal synapses. In this case, accelerated recovery from STD in mut_{KW} synapses operates in parallel to strong augmentation of release probability, which is typical for these synapses. These data indicate that dynamically regulated SV priming by Munc13s likely interfaces with other presynaptic processes and STP phenomena to shape the unique characteristics of different synapse types—throughout the brain.

STAR★METHODS

Detailed methods are provided in the online version of this paper and include the following:

- KEY RESOURCES TABLE
- RESOURCE AVAILABILITY
  - Lead contact
  - Materials availability
  - Data and code availability
- EXPERIMENTAL MODEL AND SUBJECT DETAILS
  - Mouse Generation
  - Mouse Maintenance
- METHOD DETAILS
  - Western Blot Analyses
  - Co-Immunoprecipitation Experiments
  - Immunostaining
  - Slice Preparation
  - Electrophysiology
  - Ca^{2+} Imaging in Nearly Unperturbed Terminals
- QUANTIFICATION AND STATISTICAL ANALYSIS
  - eEPSC Trains and Paired-Pulse Ratios (PPR)
  - Readily-Releasable SV Pool and Release Probability
  - Steady-State Replenishment Rate Constant ($\overline{k}+$)
  - STP at Hippocampal SC/C-CA1 Synapses

SUPPLEMENTAL INFORMATION

Supplemental information can be found online at https://doi.org/10.1016/j.neuron.2021.09.054.

ACKNOWLEDGMENTS

This work was funded by the European Commission (ERC-AdG SynPrime, N.B.) and the German Research Foundation (CNMPB, H.T. and N.B.; EXC2067/1-390729940, N.B.; SFB1286, E.N., N.B., and N.L.). We thank B.H. Cooper for advice on Munc13-1 immunolabeling and A. Zeuch, I. Herfort, and the MPI-EM DNA Core and Animal Facilities for technical support.

AUTHOR CONTRIBUTIONS

N.B. initialized the project. N.L. generated and validated Munc13-1 C_2B KIs. N.L., S.C., and H.T. designed and performed postsynaptic recordings in brainstem slices. K.-H.L. designed and performed presynaptic recordings and Ca^{2+} imaging in brainstem slices, with assistance of H.T. F.J.L.-M. designed and performed recordings in hippocampal slices and Munc13-1 immunolabeling analyses of brainstem sections, with assistance of H.T. N.L., S.C., K.-H.L., F.J.L.-M., and H.T. analyzed and interpreted data. H.T. supplied software routines and performed simulations. N.B. and E.N. provided conceptual input and advice. N.L., H.T., and N.B. wrote the manuscript. All authors provided text edits.

DECLARATION OF INTERESTS

The authors declare no competing interests. N.B. is a member of the *Neuron* advisory board.

Received: February 8, 2021
Revised: August 10, 2021
Accepted: September 23, 2021
Published: October 26, 2021

SUPPORTING CITATIONS

The following references appear in the supplemental information: Chanda and Xu-Friedman (2010); Foster et al. (2002); Neher and Sakaba (2001); Wong et al. (2003).

REFERENCES

Alabi, A.A., and Tsien, R.W. (2012). Synaptic vesicle pools and dynamics. Cold Spring Harb. Perspect. Biol. *4*, a013680.

Augustin, I., Betz, A., Herrmann, C., Jo, T., and Brose, N. (1999a). Differential expression of two novel Munc13 proteins in rat brain. Biochem. J. *337*, 363–371.

Augustin, I., Rosenmund, C., Südhof, T.C., and Brose, N. (1999b). Munc13-1 is essential for fusion competence of glutamatergic synaptic vesicles. Nature *400*, 457–461.

Betz, W.J. (1970). Depression of transmitter release at the neuromuscular junction of the frog. J. Physiol. *206*, 629–644.

Betz, A., Ashery, U., Rickmann, M., Augustin, I., Neher, E., Südhof, T.C., Rettig, J., and Brose, N. (1998). Munc13-1 is a presynaptic phorbol ester receptor that enhances neurotransmitter release. Neuron *21*, 123–136.

Borst, J.G., and Soria van Hoeve, J. (2012). The calyx of Held synapse: from model synapse to auditory relay. Annu. Rev. Physiol. *74*, 199–224.

Borst, J.G., Helmchen, F., and Sakmann, B. (1995). Pre- and postsynaptic whole-cell recordings in the medial nucleus of the trapezoid body of the rat. J. Physiol. *489*, 825–840.

Brockmann, M.M., Zarebidaki, F., Camacho, M., Grauel, M.K., Trimbuch, T., Südhof, T.C., and Rosenmund, C. (2020). A trio of active zone proteins comprised of RIM-BPs, RIMs, and Munc13s governs neurotransmitter release. Cell Rep. *32*, 107960.

Brown, D.A., and Sihra, T.S. (2008). Presynaptic signaling by heterotrimeric G-proteins. In Pharmacology of Neurotransmitter Release, T.C. Südhof and K. Starke, eds. (Springer).

Calloway, N., Gouzer, G., Xue, M., and Ryan, T.A. (2015). The active-zone protein Munc13 controls the use-dependence of presynaptic voltage-gated calcium channels. eLife *4*, e07728.

Chanda, S., and Xu-Friedman, M.A. (2010). A low-affinity antagonist reveals saturation and desensitization in mature synapses in the auditory brain stem. J. Neurophysiol. *103*, 1915–1926.

Chang, S., Reim, K., Pedersen, M., Neher, E., Brose, N., and Taschenberger, H. (2015). Complexin stabilizes newly primed synaptic vesicles and prevents their premature fusion at the mouse calyx of held synapse. J. Neurosci. *35*, 8272–8290.

Chapman, E.R., and Davis, A.F. (1998). Direct interaction of a Ca2+-binding loop of synaptotagmin with lipid bilayers. J. Biol. Chem. *273*, 13995–14001.

Chen, Z., Cooper, B., Kalla, S., Varoqueaux, F., and Young, S.M., Jr. (2013). The Munc13 proteins differentially regulate readily releasable pool dynamics and calcium-dependent recovery at a central synapse. J. Neurosci. *33*, 8336–8351.

Cho, S., Li, G.L., and von Gersdorff, H. (2011). Recovery from short-term depression and facilitation is ultrafast and Ca^{2+} dependent at auditory hair cell synapses. J. Neurosci. *31*, 5682–5692.

Davison, A.C., Hinkley, D.V., and Schechtman, E. (1986). Efficient bootstrap simulation. Biometrika *73*, 555–556.

de Jong, A.P.H., Roggero, C.M., Ho, M.R., Wong, M.Y., Brautigam, C.A., Rizo, J., and Kaeser, P.S. (2018). RIM C_2B domains target presynaptic active zone functions to PIP_2-containing membranes. Neuron *98*, 335–349.e7.

Debanne, D., Guérineau, N.C., Gähwiler, B.H., and Thompson, S.M. (1996). Paired-pulse facilitation and depression at unitary synapses in rat hippocampus: quantal fluctuation affects subsequent release. J. Physiol. *491*, 163–176.

Dimova, K., Kawabe, H., Betz, A., Brose, N., and Jahn, O. (2006). Characterization of the Munc13-calmodulin interaction by photoaffinity labeling. Biochim. Biophys. Acta *1763*, 1256–1265.

Dittman, J.S., and Regehr, W.G. (1998). Calcium dependence and recovery kinetics of presynaptic depression at the climbing fiber to Purkinje cell synapse. J. Neurosci. *18*, 6147–6162.

Dittman, J.S., Kreitzer, A.C., and Regehr, W.G. (2000). Interplay between facilitation, depression, and residual calcium at three presynaptic terminals. J. Neurosci. *20*, 1374–1385.

Dobrunz, L.E., and Stevens, C.F. (1997). Heterogeneity of release probability, facilitation, and depletion at central synapses. Neuron *18*, 995–1008.

Eggermann, E., Bucurenciu, I., Goswami, S.P., and Jonas, P. (2011). Nanodomain coupling between Ca^{2+} channels and sensors of exocytosis at fast mammalian synapses. Nat. Rev. Neurosci. *13*, 7–21.

Eguchi, K., Nakanishi, S., Takagi, H., Taoufiq, Z., and Takahashi, T. (2012). Maturation of a PKG-dependent retrograde mechanism for exoendocytic coupling of synaptic vesicles. Neuron *74*, 517–529.

Elmqvist, D., and Quastel, D.M. (1965). A quantitative study of end-plate potentials in isolated human muscle. J. Physiol. *178*, 505–529.

Farley, F.W., Soriano, P., Steffen, L.S., and Dymecki, S.M. (2000). Widespread recombinase expression using FLPeR (flipper) mice. Genesis *28*, 106–110.

Forsythe, I.D. (1994). Direct patch recording from identified presynaptic terminals mediating glutamatergic EPSCs in the rat CNS, in vitro. J. Physiol. *479*, 381–387.

Foster, K.A., Kreitzer, A.C., and Regehr, W.G. (2002). Interaction of postsynaptic receptor saturation with presynaptic mechanisms produces a reliable synapse. Neuron *36*, 1115–1126.

Frank, J.A., Yushchenko, D.A., Hodson, D.J., Lipstein, N., Nagpal, J., Rutter, G.A., Rhee, J.S., Gottschalk, A., Brose, N., Schultz, C., and Trauner, D. (2016). Photoswitchable diacylglycerols enable optical control of protein kinase C. Nat. Chem. Biol. *12*, 755–762.

Fuhrmann, G., Cowan, A., Segev, I., Tsodyks, M., and Stricker, C. (2004). Multiple mechanisms govern the dynamics of depression at neocortical synapses of young rats. J. Physiol. *557*, 415–438.

Garcia-Perez, E., and Wesseling, J.F. (2008). Augmentation controls the fast rebound from depression at excitatory hippocampal synapses. J. Neurophysiol. *99*, 1770–1786.

Gerber, S.H., Rizo, J., and Südhof, T.C. (2002). Role of electrostatic and hydrophobic interactions in $Ca^{(2+)}$-dependent phospholipid binding by the C(2)A-domain from synaptotagmin I. Diabetes *51* (*Suppl 1*), S12–S18.

Gleason, J.R. (1988). Algorithms for balanced bootstrap simulations. Am. Stat. *42*, 263–266.

Gomis, A., Burrone, J., and Lagnado, L. (1999). Two actions of calcium regulate the supply of releasable vesicles at the ribbon synapse of retinal bipolar cells. J. Neurosci. *19*, 6309–6317.

Grande, G., and Wang, L.Y. (2011). Morphological and functional continuum underlying heterogeneity in the spiking fidelity at the calyx of Held synapse in vitro. J. Neurosci. *31*, 13386–13399.

Guinan, J.J., Jr., and Li, R.Y. (1990). Signal processing in brainstem auditory neurons which receive giant endings (calyces of Held) in the medial nucleus of the trapezoid body of the cat. Hear. Res. *49*, 321–334.

Habets, R.L., and Borst, J.G. (2005). Post-tetanic potentiation in the rat calyx of Held synapse. J. Physiol. *564*, 173–187.

Hallermann, S., Fejtova, A., Schmidt, H., Weyhersmüller, A., Silver, R.A., Gundelfinger, E.D., and Eilers, J. (2010). Bassoon speeds vesicle reloading at a central excitatory synapse. Neuron *68*, 710–723.

Honigmann, A., van den Bogaart, G., Iraheta, E., Risselada, H.J., Milovanovic, D., Mueller, V., Müllar, S., Diederichsen, U., Fasshauer, D., Grubmüller, H., et al. (2013). Phosphatidylinositol 4,5-bisphosphate clusters act as molecular beacons for vesicle recruitment. Nat. Struct. Mol. Biol. *20*, 679–686.

Hooper, M., Hardy, K., Handyside, A., Hunter, S., and Monk, M. (1987). HPRT-deficient (Lesch-Nyhan) mouse embryos derived from germline colonization by cultured cells. Nature *326*, 292–295.

Hosoi, N., Sakaba, T., and Neher, E. (2007). Quantitative analysis of calcium-dependent vesicle recruitment and its functional role at the calyx of Held synapse. J. Neurosci. *27*, 14286–14298.

Imig, C., Min, S.W., Krinner, S., Arancillo, M., Rosenmund, C., Südhof, T.C., Rhee, J., Brose, N., and Cooper, B.H. (2014). The morphological and molecular nature of synaptic vesicle priming at presynaptic active zones. Neuron *84*, 416–431.

Ishikawa, T., Nakamura, Y., Saitoh, N., Li, W.B., Iwasaki, S., and Takahashi, T. (2003). Distinct roles of Kv1 and Kv3 potassium channels at the calyx of Held presynaptic terminal. J. Neurosci. *23*, 10445–10453.

Iwasaki, S., and Takahashi, T. (2001). Developmental regulation of transmitter release at the calyx of Held in rat auditory brainstem. J. Physiol. *534*, 861–871.

Joshi, I., and Wang, L.Y. (2002). Developmental profiles of glutamate receptors and synaptic transmission at a single synapse in the mouse auditory brainstem. J. Physiol. *540*, 861–873.

Joshi, I., Shokralla, S., Titis, P., and Wang, L.Y. (2004). The role of AMPA receptor gating in the development of high-fidelity neurotransmission at the calyx of Held synapse. J. Neurosci. *24*, 183–196.

Jung, N., and Haucke, V. (2007). Clathrin-mediated endocytosis at synapses. Traffic *8*, 1129–1136.

Junge, H.J., Rhee, J.S., Jahn, O., Varoqueaux, F., Spiess, J., Waxham, M.N., Rosenmund, C., and Brose, N. (2004). Calmodulin and Munc13 form a Ca^{2+} sensor/effector complex that controls short-term synaptic plasticity. Cell *118*, 389–401.

Kabachinski, G., Yamaga, M., Kielar-Grevstad, D.M., Bruinsma, S., and Martin, T.F. (2014). CAPS and Munc13 utilize distinct PIP2-linked mechanisms to promote vesicle exocytosis. Mol. Biol. Cell *25*, 508–521.

Kaeser, P.S., and Regehr, W.G. (2017). The readily releasable pool of synaptic vesicles. Curr. Opin. Neurobiol. *43*, 63–70.

Koike-Tani, M., Saitoh, N., and Takahashi, T. (2005). Mechanisms underlying developmental speeding in AMPA-EPSC decay time at the calyx of Held. J. Neurosci. *25*, 199–207.

Kopp-Scheinpflug, C., Tolnai, S., Malmierca, M.S., and Rübsamen, R. (2008). The medial nucleus of the trapezoid body: comparative physiology. Neuroscience *154*, 160–170.

Korogod, N., Lou, X., and Schneggenburger, R. (2005). Presynaptic Ca^{2+} requirements and developmental regulation of posttetanic potentiation at the calyx of Held. J. Neurosci. *25*, 5127–5137.

Kushmerick, C., Renden, R., and von Gersdorff, H. (2006). Physiological temperatures reduce the rate of vesicle pool depletion and short-term depression via an acceleration of vesicle recruitment. J. Neurosci. *26*, 1366–1377.

Lai, Y., Choi, U.B., Leitz, J., Rhee, H.J., Lee, C., Altas, B., Zhao, M., Pfuetzner, R.A., Wang, A.L., Brose, N., et al. (2017). Molecular mechanisms of synaptic vesicle priming by Munc13 and Munc18. Neuron *95*, 591–607.e10.

Lee, J.S., Ho, W.K., Neher, E., and Lee, S.H. (2013). Superpriming of synaptic vesicles after their recruitment to the readily releasable pool. Proc. Natl. Acad. Sci. USA *110*, 15079–15084.

Li, L., Bischofberger, J., and Jonas, P. (2007). Differential gating and recruitment of P/Q-, N-, and R-type Ca^{2+} channels in hippocampal mossy fiber boutons. J. Neurosci. *27*, 13420–13429.

Lin, K.H., Taschenberger, H., and Neher, E. (2017). Dynamics of volume-averaged intracellular Ca^{2+} in a rat CNS nerve terminal during single and repetitive voltage-clamp depolarizations. J. Physiol. *595*, 3219–3236.

Lindau, M., and Neher, E. (1988). Patch-clamp techniques for time-resolved capacitance measurements in single cells. Pflugers Arch. *411*, 137–146.

Lipstein, N., Schaks, S., Dimova, K., Kalkhof, S., Ihling, C., Kölbel, K., Ashery, U., Rhee, J., Brose, N., Sinz, A., and Jahn, O. (2012). Nonconserved Ca^{2+}/calmodulin binding sites in Munc13s differentially control synaptic short-term plasticity. Mol. Cell. Biol. *32*, 4628–4641.

Lipstein, N., Sakaba, T., Cooper, B.H., Lin, K.H., Strenzke, N., Ashery, U., Rhee, J.S., Taschenberger, H., Neher, E., and Brose, N. (2013). Dynamic control of synaptic vesicle replenishment and short-term plasticity by $Ca^{(2+)}$-calmodulin-Munc13-1 signaling. Neuron *79*, 82–96.

Liu, X., Seven, A.B., Camacho, M., Esser, V., Xu, J., Trimbuch, T., Quade, B., Su, L., Ma, C., Rosenmund, C., and Rizo, J. (2016). Functional synergy between the Munc13 C-terminal C1 and C2 domains. eLife *5*, e13696.

Lorteije, J.A., Rusu, S.I., Kushmerick, C., and Borst, J.G. (2009). Reliability and precision of the mouse calyx of Held synapse. J. Neurosci. *29*, 13770–13784.

Lou, X., Korogod, N., Brose, N., and Schneggenburger, R. (2008). Phorbol esters modulate spontaneous and Ca2+-evoked transmitter release via acting on both Munc13 and protein kinase C. J. Neurosci. *28*, 8257–8267.

Ma, C., Li, W., Xu, Y., and Rizo, J. (2011). Munc13 mediates the transition from the closed syntaxin-Munc18 complex to the SNARE complex. Nat. Struct. Mol. Biol. *18*, 542–549.

Malagon, G., Miki, T., Tran, V., Gomez, L.C., and Marty, A. (2020). Incomplete vesicular docking limits synaptic strength under high release probability conditions. eLife *9*, e52137.

Malenka, R.C., Ayoub, G.S., and Nicoll, R.A. (1987). Phorbol esters enhance transmitter release in rat hippocampal slices. Brain Res. *403*, 198–203.

Michelassi, F., Liu, H., Hu, Z., and Dittman, J.S. (2017). A C1-C2 module in Munc13 inhibits calcium-dependent neurotransmitter release. Neuron *95*, 577–590.e5.

Milosevic, I., Sørensen, J.B., Lang, T., Krauss, M., Nagy, G., Haucke, V., Jahn, R., and Neher, E. (2005). Plasmalemmal phosphatidylinositol-4,5-bisphosphate level regulates the releasable vesicle pool size in chromaffin cells. J. Neurosci. *25*, 2557–2565.

Miyano, R., Miki, T., and Sakaba, T. (2019). Ca-dependence of synaptic vesicle exocytosis and endocytosis at the hippocampal mossy fibre terminal. J. Physiol. *597*, 4373–4386.

Mizuseki, K., and Buzsáki, G. (2013). Preconfigured, skewed distribution of firing rates in the hippocampus and entorhinal cortex. Cell Rep. *4*, 1010–1021.

Müller, M., Felmy, F., Schwaller, B., and Schneggenburger, R. (2007). Parvalbumin is a mobile presynaptic Ca^{2+} buffer in the calyx of Held that accelerates the decay of Ca^{2+} and short-term facilitation. J. Neurosci. *27*, 2261–2271.

Neher, E. (2015). Merits and limitations of vesicle pool models in view of heterogeneous populations of synaptic vesicles. Neuron *87*, 1131–1142.

Neher, E., and Sakaba, T. (2001). Combining deconvolution and noise analysis for the estimation of transmitter release rates at the calyx of held. J. Neurosci. *21*, 444–461.

Neher, E., and Sakaba, T. (2008). Multiple roles of calcium ions in the regulation of neurotransmitter release. Neuron *59*, 861–872.

Pinheiro, P.S., Houy, S., and Sørensen, J.B. (2016). C2-domain containing calcium sensors in neuroendocrine secretion. J. Neurochem. *139*, 943–958.

Piotrowski, C., Moretti, R., Ihling, C.H., Haedicke, A., Liepold, T., Lipstein, N., Meiler, J., Jahn, O., and Sinz, A. (2020). Delineating the molecular basis of the calmodulin–bMunc13-2 interaction by cross-linking/mass spectrometry-evidence for a novel CaM binding motif in bMunc13-2. Cells *9*, 136.

Pyott, S.J., and Rosenmund, C. (2002). The effects of temperature on vesicular supply and release in autaptic cultures of rat and mouse hippocampal neurons. J. Physiol. *539*, 523–535.

Quade, B., Camacho, M., Zhao, X., Orlando, M., Trimbuch, T., Xu, J., Li, W., Nicastro, D., Rosenmund, C., and Rizo, J. (2019). Membrane bridging by Munc13-1 is crucial for neurotransmitter release. eLife *8*, e42806.

Renden, R., Taschenberger, H., Puente, N., Rusakov, D.A., Duvoisin, R., Wang, L.Y., Lehre, K.P., and von Gersdorff, H. (2005). Glutamate transporter studies reveal the pruning of metabotropic glutamate receptors and absence of AMPA receptor desensitization at mature calyx of Held synapses. J. Neurosci. *25*, 8482–8497.

Rhee, J.S., Betz, A., Pyott, S., Reim, K., Varoqueaux, F., Augustin, I., Hesse, D., Südhof, T.C., Takahashi, M., Rosenmund, C., and Brose, N. (2002). Beta phorbol ester- and diacylglycerol-induced augmentation of transmitter release is mediated by Munc13s and not by PKCs. Cell *108*, 121–133.

Ritzau-Jost, A., Jablonski, L., Viotti, J., Lipstein, N., Eilers, J., and Hallermann, S. (2018). Apparent calcium dependence of vesicle recruitment. J. Physiol. *596*, 4693–4707.

Sakaba, T. (2006). Roles of the fast-releasing and the slowly releasing vesicles in synaptic transmission at the calyx of Held. J. Neurosci. *26*, 5863–5871.

Sakaba, T., and Neher, E. (2001a). Calmodulin mediates rapid recruitment of fast-releasing synaptic vesicles at a calyx-type synapse. Neuron *32*, 1119–1131.

Sakaba, T., and Neher, E. (2001b). Quantitative relationship between transmitter release and calcium current at the calyx of held synapse. J. Neurosci. *21*, 462–476.

Sakamoto, H., Ariyoshi, T., Kimpara, N., Sugao, K., Taiko, I., Takikawa, K., Asanuma, D., Namiki, S., and Hirose, K. (2018). Synaptic weight set by Munc13-1 supramolecular assemblies. Nat. Neurosci. *21*, 41–49.

Schneggenburger, R., and Forsythe, I.D. (2006). The calyx of Held. Cell Tissue Res. *326*, 311–337.

Schneggenburger, R., Meyer, A.C., and Neher, E. (1999). Released fraction and total size of a pool of immediately available transmitter quanta at a calyx synapse. Neuron *23*, 399–409.

Schneider, C.A., Rasband, W.S., and Eliceiri, K.W. (2012). NIH Image to ImageJ: 25 years of image analysis. Nat. Methods *9*, 671–675.

Shin, O.H., Lu, J., Rhee, J.S., Tomchick, D.R., Pang, Z.P., Wojcik, S.M., Camacho-Perez, M., Brose, N., Machius, M., Rizo, J., et al. (2010). Munc13 C2B domain is an activity-dependent Ca2+ regulator of synaptic exocytosis. Nat. Struct. Mol. Biol. *17*, 280–288.

Sigler, A., Oh, W.C., Imig, C., Altas, B., Kawabe, H., Cooper, B.H., Kwon, H.B., Rhee, J.S., and Brose, N. (2017). Formation and maintenance of functional spines in the absence of presynaptic glutamate release. Neuron *94*, 304–311.e4.

Siksou, L., Varoqueaux, F., Pascual, O., Triller, A., Brose, N., and Marty, S. (2009). A common molecular basis for membrane docking and functional priming of synaptic vesicles. Eur. J. Neurosci. *30*, 49–56.

Stevens, C.F., and Tsujimoto, T. (1995). Estimates for the pool size of releasable quanta at a single central synapse and for the time required to refill the pool. Proc. Natl. Acad. Sci. USA *92*, 846–849.

Stevens, C.F., and Wesseling, J.F. (1998). Activity-dependent modulation of the rate at which synaptic vesicles become available to undergo exocytosis. Neuron *21*, 415–424.

Taschenberger, H., and von Gersdorff, H. (2000). Fine-tuning an auditory synapse for speed and fidelity: developmental changes in presynaptic waveform, EPSC kinetics, and synaptic plasticity. J. Neurosci. *20*, 9162–9173.

Taschenberger, H., Leão, R.M., Rowland, K.C., Spirou, G.A., and von Gersdorff, H. (2002). Optimizing synaptic architecture and efficiency for high-frequency transmission. Neuron *36*, 1127–1143.

Taschenberger, H., Woehler, A., and Neher, E. (2016). Superpriming of synaptic vesicles as a common basis for intersynapse variability and modulation of synaptic strength. Proc. Natl. Acad. Sci. USA *113*, E4548–E4557.

Thomas, K.R., and Capecchi, M.R. (1987). Site-directed mutagenesis by gene targeting in mouse embryo-derived stem cells. Cell *51*, 503–512.

Traynelis, S.F. (1998). Software-based correction of single compartment series resistance errors. J. Neurosci. Methods *86*, 25–34.

van den Bogaart, G., Meyenberg, K., Risselada, H.J., Amin, H., Willig, K.I., Hubrich, B.E., Dier, M., Hell, S.W., Grubmüller, H., Diederichsen, U., and Jahn, R. (2011). Membrane protein sequestering by ionic protein-lipid interactions. Nature *479*, 552–555.

van den Bogaart, G., Meyenberg, K., Diederichsen, U., and Jahn, R. (2012). Phosphatidylinositol 4,5-bisphosphate increases Ca2+ affinity of synaptotagmin-1 by 40-fold. J. Biol. Chem. *287*, 16447–16453.

Varoqueaux, F., Sigler, A., Rhee, J.S., Brose, N., Enk, C., Reim, K., and Rosenmund, C. (2002). Total arrest of spontaneous and evoked synaptic transmission but normal synaptogenesis in the absence of Munc13-mediated vesicle priming. Proc. Natl. Acad. Sci. USA *99*, 9037–9042.

Varoqueaux, F., Sons, M.S., Plomp, J.J., and Brose, N. (2005). Aberrant morphology and residual transmitter release at the Munc13-deficient mouse neuromuscular synapse. Mol Cell Biol *25*, 5973–5984. https://doi.org/10.1128/MCB.25.14.5973-5984.2005.

von Gersdorff, H., and Borst, J.G. (2002). Short-term plasticity at the calyx of Held. Nat. Rev. Neurosci. *3*, 53–64.

von Gersdorff, H., Schneggenburger, R., Weis, S., and Neher, E. (1997). Presynaptic depression at a calyx synapse: the small contribution of metabotropic glutamate receptors. J. Neurosci. *17*, 8137–8146.

Wadiche, J.I., and Jahr, C.E. (2001). Multivesicular release at climbing fiber-Purkinje cell synapses. Neuron *32*, 301–313.

Walter, A.M., Müller, R., Tawfik, B., Wierda, K.D., Pinheiro, P.S., Nadler, A., McCarthy, A.W., Ziomkiewicz, I., Kruse, M., Reither, G., et al. (2017). Phosphatidylinositol 4,5-bisphosphate optical uncaging potentiates exocytosis. eLife *6*, e30203.

Wang, L.Y., and Kaczmarek, L.K. (1998). High-frequency firing helps replenish the readily releasable pool of synaptic vesicles. Nature *394*, 384–388.

Wang, Y., and Manis, P.B. (2008). Short-term synaptic depression and recovery at the mature mammalian endbulb of Held synapse in mice. J. Neurophysiol. *100*, 1255–1264.

Wesseling, J.F., and Lo, D.C. (2002). Limit on the role of activity in controlling the release-ready supply of synaptic vesicles. J. Neurosci. *22*, 9708–9720.

Wierda, K.D., Toonen, R.F., de Wit, H., Brussaard, A.B., and Verhage, M. (2007). Interdependence of PKC-dependent and PKC-independent pathways for presynaptic plasticity. Neuron *54*, 275–290.

Wong, A.Y., Graham, B.P., Billups, B., and Forsythe, I.D. (2003). Distinguishing between presynaptic and postsynaptic mechanisms of short-term depression during action potential trains. J. Neurosci. *23*, 4868–4877.

Yang, H., and Xu-Friedman, M.A. (2008). Relative roles of different mechanisms of depression at the mouse endbulb of Held. J. Neurophysiol. *99*, 2510–2521.

Zhang, X., Rizo, J., and Südhof, T.C. (1998). Mechanism of phospholipid binding by the C_2A-domain of synaptotagmin I. Biochemistry *37*, 12395–12403.

Zikich, D., Mezer, A., Varoqueaux, F., Sheinin, A., Junge, H.J., Nachliel, E., Melamed, R., Brose, N., Gutman, M., and Ashery, U. (2008). Vesicle priming and recruitment by ubMunc13-2 are differentially regulated by calcium and calmodulin. J. Neurosci. *28*, 1949–1960.

Zucker, R.S., and Regehr, W.G. (2002). Short-term synaptic plasticity. Annu. Rev. Physiol. *64*, 355–405.

STAR★METHODS

KEY RESOURCES TABLE

REAGENT or RESOURCE	SOURCE	IDENTIFIER
Antibodies		
Anti-Bassoon antibody	Enzo Life Sciences	Cat# SAP7F407; RRID: AB_2313990
Anti-Calmodulin antibody	Upstate Biotechnology	Cat# 05-173; RRID: AB_309644
Anti-CAPS 1 antibody	Synaptic Systems	Cat# 262 013; RRID: AB_2619979
Anti-Doc 2b antibody	Synaptic Systems	Cat# 174 103; RRID: AB_2619874
MAP2 Antibody	Novus	Cat# NB300-213; RRID: AB_2138178
Anti-Munc13-1, rabbit polyclonal	Generated in house	41
Anti-Munc13-1, mouse monoclonal	Generated in house	3H5; Betz et al., 1998
Anti-ubMunc13-2, rabbit polyclonal	Generated in house	48
Anti-bMunc13-2, rabbit polyclonal	Generated in house	50
Anti-Munc13-3, rabbit polyclonal	Generated in house	52
Anti-Munc13-1 antibody	Synaptic Systems	Cat# 126 103; RRID: AB_887733
Anti-Munc18-1 antibody	Synaptic Systems	Cat# 116 002; RRID: AB_887736
Anti-Rim1, rabbit polyclonal	Generated in house	Q703
Anti-SNAP 25 antibody	Synaptic Systems	Cat# 111 011; RRID: AB_887794
Anti-Synapsin 1 antibody	Synaptic Systems	Cat# 106 011; RRID: AB_2619772
Anti-Synaptobrevin 2 antibody	Synaptic Systems	Cat# 104 211; RRID: AB_887811
Anti-Synaptotagmin 1 antibody	Synaptic Systems	Cat# 105 001; RRID: AB_887831
Anti-Syntaxin 1 antibody	Synaptic Systems	Cat# 110 011; RRID: AB_887844
Peroxidase-AffiniPure Goat Anti-Mouse IgG (H+L) antibody	Jackson ImmunoResearch Labs	Cat# 115-035-146; RRID:AB_2307392
Peroxidase-AffiniPure Goat Anti-Rabbit IgG (H+L) antibody	Jackson ImmunoResearch Labs	Cat# 111-035-144; RRID:AB_2307391
Goat anti-rabbit IgG Secondary Antibody, Alexa Fluor 488	Thermo Fisher Scientific	Cat# A-11008; RRID: AB_143165
Goat anti-mouse IgG Secondary Antibody, Alexa 555	Thermo Fisher Scientific	Cat# A21424; RRID: AB_141780
Goat anti-Chicken Secondary Antibody, Alexa Fluor 633	Invitrogen	Cat# A-21103; RRID: AB_2535756
Chemicals, peptides, and recombinant proteins		
2,3-Dioxo-6-nitro-1,2,3,4-tetrahydrobenzo [*f*]quinoxaline-7-sulfonamide disodium salt (NBQX)	HelloBio	Cat# HB0443
Goat Serum	GIBCO	Cat# 16210-072
Kynurenic acid	Sigma-Aldrich	Cat# K3375
MemCode™ Reversible Protein Stain Kit	Thermo Scientific	Cat# 24580
Mounting glue: Aqua-Poly/Mount	Polysciences	Cat# 18606-20
Paraformaldehyde (PFA)	Serva	Cat# 31628.02
Phorbol-12,13-dibutyrate (PDBu)	Calbiochem	Cat# 524390
Recombinant Protein G - Sepharose 4B	Invitrogen	Cat# 101242
Strychnine hydrochloride	Tocris Bioscience	Cat# 2785
Tetraethylammonium chloride (TEA)	Sigma Aldrich	Cat# T-2265
Triton X-100	Roche	Cat# 10789704001
Experimental models: Cell lines		
Mouse: 129/ola embryonic stem cell line E14	Hooper et al., 1987	N/A

(*Continued on next page*)

Continued

REAGENT or RESOURCE	SOURCE	IDENTIFIER
Experimental models: Organisms/strains		
Mouse: Unc13a^{tm5Bros}	This manuscript	C2BDN
Mouse: Unc13a^{tm6Bros}	This manuscript	C2BKW
Mouse: Unc13a$^{tm4.1Bros}$	Generated in house	Lipstein et al., 2013
Mouse: C57BL/6NCrL	Charles River Laboratories	RRID:IMSR_CRL:027
Mouse Gt(ROSA)26Sor$^{tm1(FLP1)Dym}$	Breeding in house	Farley et al., 2000
Oligonucleotides		
Sense prime: 5′-GGGTAGCTGCAGGATTTATTGTAT-3′	Generated in house	25254, *UNC13A* gene intron 18
Antisense prime: 5′-TGTGTCCAGTTTCAGAGGTC-3′	Generated in house	35776, *UNC13A* gene intron 19
Recombinant DNA		
Plasmid: pTKPuroFRT-*UNC13A* Exons 13-26 Exon 18*^{C2BDN}	Cloned in house	N/A
Plasmid: pTKPuroFRT-*UNC13A* Exons 13-26 C2BKW*^{C2BKW}	Cloned in house	N/A
Software and algorithms		
GraphPad Prism 8	GraphPad Software	https://www.graphpad.com; RRID: SCR_002798
IgorPro 6.3.7.2	Wavemetrics	https://www.wavemetrics.com; RRID: SCR_000325
ImageJ	National Institutes of Health	https://imagej.nih.gov/ij; RRID: SCR_003070
Microsoft Excel	Microsoft	https://www.microsoft.com/en-us/; RRID:SCR_016137
PatchMaster v2x53/ Pulse v8.80	HEKA / Harvard Bioscience	https://www.heka.com; RRID: SCR_000034
Python based Relational Animal Tracking	Scionics Computer Innovation GmbH	https://www.scionics.com/pyrat.html; RRID:SCR_021014
R: A Language and Environment for Statistical Computing	R Core Team	http://www.r-project.org/; RRID:SCR_001905
Other		
Beckman Ultracentrifuge L-70	Beckman	N/A
Borosilicate glass with filament	Science Products	GB150F-8P
Cryostat	Leica	RRID:SCR_016844
EPC 10 double patch clamp amplifier	HEKA Elektronik	RRID:SCR_018399
Leica TCS SP5 II microscope	Leica	RRID:SCR_018714
Vibratome VT1000S Leica	Leica	RRID:SCR_016495
Olympus BX51 microscope	Olympus	RRID:SCR_018949

RESOURCE AVAILABILITY

Lead contact

Further information and requests for resources and reagents should be directed to and will be fulfilled by the lead contact, Nils Brose (Brose@em.mpg.de).

Materials availability

Mouse lines will be shared upon request within the limits of the respective material transfer agreements.

Data and code availability

- Any raw data obtained in the present study are available from the lead contact upon request.
- The study did not generate any code.
- Any additional information required to reanalyse the data reported in this paper is available from the lead contact upon request.

EXPERIMENTAL MODEL AND SUBJECT DETAILS

Mouse Generation

The Munc13-1 knock-in (KI) mice were generated by homologous recombination in 129/ola embryonic stem cells (Hooper et al., 1987). A targeting vector containing UNC13A exons 13-26 with an insertion of an FRT-Puromycin-FRT cassette before exon 18 (Figure 1A) was cloned. To create the C2BDN line, three nucleotide exchanges were included, two leading to the exchange of aspartic acid residues in position 705 and 711 of Munc13-1 to asparagine (GAC to AAC), and one that eliminates a nearby BamHI site (GGA to GGC) but preserves the glycine residue (pTKPuroFRT-*UNC13A* Exons 13-26 Exon 18*^{C2BDN}; Figures 1A and 1D). To create the C2BKW line, the targeting vector included two nucleotide exchanges, one leading to the replacement of a lysine residues in position 706 of Munc13-1 by a tryptophan (AAG to TGG), and one to eliminate a nearby BamHI site (GGA to GGC), preserving the glycine residue (pTKPuroFRT-*UNC13A* Exons 13-26 Exon 18*^{C2BKW}; Figures 1A and 1D). The resulting vectors were used to electroporate stem cells, and the correct genomic integration of the cassette was identified by the acquisition of puromycin resistance (Thomas and Capecchi, 1987), and by long-range PCR amplification and DNA sequencing. Positive clones were amplified, injected into blastocysts, and the resulting mice were screened for germline transmission via long-range PCR amplification. To eliminate the puromycin resistance cassette, mice were crossed with Gt(ROSA)26Sor$^{tm1(FLP1)Dym}$ mice (Farley et al., 2000). Offspring were analyzed using genotyping PCR (Sense prime: 5′-GGGTAGCTGCAGGATTTATTGTAT-3′; Antisense prime: 5′-TGTGTCCAGTTTCAGAGGTC-3′), and sequencing (Figures 1B–1D), and animals in which a successful cre recombination had occurred were selected for further breeding with C57BL/6N mice for three generations. Mice were then cross-bred to produce homozygous and wt littermates for experiments.

Mouse Maintenance

Mutant mouse generation and animal experiments were approved by the responsible authorities of the local government (Lower Saxony State Office for Consumer Protection and Food Safety (LAVES; permit 33.19-42502-04-15/1817). Animals were maintained in groups in accordance with European Union Directive 63/2010/EU and ETS. Animal health was controlled daily by caretakers and by a veterinarian, and a quarterly health monitoring was done according to FELASA recommendations with either NMRI sentinel mice or animals from the colony (serological analyses; microbiological, parasitological, and pathological examinations). Abnormal findings were not made during the period of the study. Mice were kept in individually ventilated cages, under specific pathogen-free conditions, 21 ± 1°C, 55% relative humidity, 12 h/12 h light/dark cycle). Food and tap water, as well as bedding and nesting material, were provided *ad libitum*, and cages were changed once a week. P14–17 littermate homozygous Munc13-1 KI mice and wt controls of either sex were analyzed. Littermates were used to minimize effects of genetic background, although only minor differences were observed between wt lines (Table S1). Mice were routinely genotyped by PCR (Figures 1B–1D). We did not observe large deviations from the expected Mendelian ratios among offspring, although for C2BKW mice a slightly lower than expected fraction of homozygous KI mice was obtained, possibly indicating a slightly increased perinatal lethality. C57BL/6N mice were used for the experiments shown in Figures 6D, S3B, S3C, and S7.

METHOD DETAILS

Western Blot Analyses

P2 crude synaptosomal fractions were obtained from cortical brain tissue of P16 KI mice and wt littermates as previously described (Lipstein et al., 2013). Between 2-20 μg protein were separated on 4%–12% gradient Bis-Tris polyacrylamide gels (Invitrogen) and blotted onto nitrocellulose membranes. The protein load per lane was quantified by a reversible membrane staining protocol (MemCode; Pierce) and quantified using ImageJ. The following antibodies were subsequently used to identify the indicated proteins: rabbit polyclonal (rp) anti-Munc13-1 (40), anti-ubMunc13-2, and anti-bMunc13-2 (Varoqueaux et al., 2005), rp-anti-Doc2 (SySy; 174 103), rp-anti-CAPS-1 (SySy 262 013), rp-anti-Munc18-1 (SySy; 116 002), mouse monoclonal (mm)-anti Synapsin 1 (SySy 106 011), mm-anti-Syntaxin 1A/B (SySy 110 011), mm-anti-Synaptobrevin 2 (SySy 104 211), mm-anti-Synaptotagmin (SySy 105 001), rp anti-Rim (lab antibody; Q703), mm anti-SNAP25 (SySy; 111 011). After incubation with corresponding secondary antibodies (Peroxidase-AffiniPure Goat Anti-Mouse IgG or peroxidase-AffiniPure Goat Anti-Rabbit IgG antibody), the western blot signal was detected with an INTAS imager (INTAS Science Imaging), quantified using ImageJ, and normalized to the protein load. Between 3-4 independent analyses were preformed per condition. Quantification is presented as mean ± SEM.

Co-Immunoprecipitation Experiments

Co-immunoprecipitation was performed according to Lipstein et al. (2013). Briefly, crude synaptosomal fractions obtained from cerebral corti of adult (8–11 weeks) wt and KI mice were solubilized and ultracentrifuged using a Beckmann L-70 at 100,000 g to remove

insoluble material. A sample ('input') was collected, and the remaining fraction was incubated with a rp-anti-Munc13-1 (40). Sepharose-Protein G beads (Invitrogen) were added to capture the antibody and associated proteins, washed to remove background, and eluted using denaturating Laemmli buffer ('IP' samples). The samples were loaded on 4%–12% gradient Bis-Tris polyacrylamide gels and blotted according to a modified version of the Sigma protocol (product C7055) with mm-anti-Calmodulin (Upstate Biotechnology). Munc13-1 was blotted using the mm-anti Munc13-1 (3H5; Betz et al., 1998).

Immunostaining

Immunostaining experiments were performed on P15 coronal brainstem sections using primary antibodies against Munc13-1, Bassoon, and MAP-2. Brains were rapidly frozen in isopentane (−35°C). Sixteen μm-thick coronal cryosections of the MNTB region were cut and mounted on Superfrost slides, air-dried for 15 min, and immersion-fixed in ice-cold 4% paraformaldehyde solution (4% PFA in 0.1 M PB, pH 7.4) for 5 min at room temperature (RT). To ensure similar fixation and labeling conditions between genotypes, sections of mutant and corresponding wt mice were mounted together. Sections were incubated for 90 min at RT in blocking solution (0.1 M PB, 5% normal goat serum, 0.1% cold water fish skin gelatine, 0.5% Triton X-100, pH 7.4) before being treated overnight at 4°C with the primary antibodies rp-anti-Munc13-1 Ab (SySy 126 103, 1:400), mm-anti-Bassoon (Enzo Life Sciences SAP7F407 1:400), and chicken polyclonal anti-MAP2 (Novus NB300-213, 1:600), diluted in incubation buffer (0.1 M PB, 3% normal goat serum, 0.1% cold water fish skin gelatine, 0.3% Triton X-100, pH 7.4). After washing in PB, sections were incubated for 2 h at RT in the dark with the fluorescent secondary antibodies Alexa 488-coupled goat anti-rabbit, Alexa-555-coupled goat anti-mouse, and Alexa-633-coupled goat anti-chicken (Invitrogen, 1:1000) diluted in incubation buffer. Coverslips were mounted with Aqua-PolyMount (Polysciences). Confocal laser scanning micrographs of presynaptic compartments surrounding MNTB PNs were acquired with a Leica TCS SP5 II confocal microscope. An HCX PL APO lambda blue 63 × water immersion objective (NA = 1.2) and a pinhole setting of 0.38 AU were used to obtain single-plane micrographs (512 × 512; x-y pixel spacing = 48.1 nm) in sequential scanning mode. Laser power and gain were adjusted to ensure that signals were in the linear range of detection. Confocal images were subjected to deconvolution using two ImageJ (National Institutes of Health; Bethesda, MD) plugins: point spread functions were generated using -Diffraction PSF 3D plugin, and deconvolution was performed using DeconvolutionLab plugin (Biomedical Imaging Group, EPFL; Lausanne, Switzerland). Individual Munc13-1 immunoreactive puncta were detected using a thresholding algorithm (ImageJ). For all Munc13-1-positive puncta within ~1 μm wide regions of interest (ROIs) drawn around the perimeter of MNTB PNs and approximately delineating the presynaptic compartments, the center of mass was determined and those coordinates were exported for further processing. For each ROI, the average density of Munc13-1-positive puncta per μm perimeter was obtained and the mean nearest-neighbor distance was calculated as a parameter characterizing the distribution of Munc13-1-positive puncta within a given ROI.

Slice Preparation

Acute brainstem slices of postnatal (P14–P17) mice of either sex were prepared as previously described (Chang et al., 2015). After decapitation, brains were immersed in ice-cold low-Ca^{2+} artificial CSF (aCSF) containing (in mM): 125 NaCl, 2.5 KCl, 0.1 $CaCl_2$, 3 $MgCl_2$, 25 glucose, 25 $NaHCO_3$, 1.25 NaH_2PO_4, 0.4 ascorbic acid, 3 myoinositol, and 2 Na-pyruvate (pH 7.4, bubbled with 95% O_2, 5% CO_2). The brainstem was glued onto the stage of a VT1000S vibratome (Leica), and 200 μm-thick coronal slices containing the medial nucleus of the trapezoid body (MNTB) were cut. Slices were incubated for 40 min at 35°C in a chamber containing normal aCSF (identical to low-Ca^{2+} aCSF, except that 3 mM $MgCl_2$ and 0.1 mM $CaCl_2$ were replaced with 1.3 mM $MgCl_2$ and 1.7 mM $CaCl_2$). Slices were kept at RT (21–24°C) for up to 5 h after recovery.

Acute parasagittal hippocampal slices (300 μm thick) were prepared from P16–P21 mice of either sex using a VT1000S vibratome and ice-cold low-Ca^{2+}/high-Mg^{2+} sucrose-based cutting solution containing (in mM): 120 sucrose, 64 NaCl, 25 $NaHCO_3$, 2.5 KCl, 1.25 NaH_2PO_4, 10 glucose, 0.5 $CaCl_2$ and 7 $MgCl_2$ (pH 7.4, bubbled with 95% O_2, 5% CO_2). Slices were incubated for 40 min at 35°C in a chamber filled with normal aCSF containing 1 mM $MgCl_2$ and 2 mM $CaCl_2$. Slices were kept at RT for up to 5 h after recovery.

Electrophysiology

Whole-cell patch-clamp recordings were made from calyx of Held terminals and principal neurons (PNs) of the MNTB at RT using a EPC-10 amplifier controlled by Pulse or PatchMaster software (HEKA Elektronik). Patch-pipettes (Science Products) were coated with dental wax in order to minimize fast capacitive transients during voltage-clamp experiments and to reduce stray capacitance.

For postsynaptic recordings, pipettes with an open-tip resistance of 2.5–4 MΩ were filled with a solution containing (in mM): 100 K-gluconate, 60 KCl, 5 Na_2-phosphocreatine, 10 HEPES, 5 EGTA, 0.3 Na_2-GTP, and 4 ATP-Mg, pH 7.3, with KOH. During experiments, slices were continuously perfused with normal aCSF solution containing 1.3 mM $MgCl_2$ and 1.7 mM $CaCl_2$ and supplemented with 5 μM strychnine, to block glycinergic inputs. Cells were visualized by infrared-differential interference contrast microscopy through a 40X water-immersion objective using an upright BX51WI microscope (Olympus). All experiments were performed at RT. A bipolar stimulation electrode was used to evoke presynaptic APs (stimulus intensity ≤ 20 V, 100 μs duration). Series resistance (R_s) was ≤ 8 MΩ and compensated ≥ 82%. Holding potential (V_h) and leak current were −70 mV and ≤ 200 pA, respectively. Sampling interval and low-pass filter settings were 20 μs and 5.0 kHz, respectively. eEPSC peaks measured in P14-17 mouse calyx synapses frequently exceed amplitudes of 10 nA (Chang et al., 2015; Joshi and Wang, 2002). Assuming a maximum R_s = 8 MΩ that is 80% compensated by the amplifier R_s-compensation circuitry, such peak amplitudes cause a transient voltage escape that corresponds to a > 20% drop in driving force at V_h = −70 mV for a synaptic conductance having a reversal potential of ~0 mV. To reduce

eEPSC amplitudes for improved voltage-clamp and in order to attenuate postsynaptic AMPAR saturation and AMPAR desensitization, all experiments were performed in the continuous presence of 1 mM of the low-affinity GluR antagonist kynurenic acid (kyn), unless explicitly stated otherwise. The blocking ratio $eEPSC_{kyn}/eEPSC_{ctrl}$ is shown for a subset of the experiments in Figure S1. Furthermore, voltage-clamp errors caused by remaining uncompensated R_s were corrected offline by a software routine (see offline analysis).

Presynaptic voltage-clamp recordings were performed using patch pipettes with an open-tip resistance of 3–4.5 MΩ. Series resistance was $\leq$ 15 MΩ and R_s was compensated 60%–65%. For measuring $I_{Ca(V)}$ and membrane capacitance (ΔC_m), pipettes were filled with a Cs-gluconate based solution containing (in mM): 100 Cs-gluconate, 30 TEA-Cl, 30 CsCl, 10 HEPES, 0.05 EGTA, 5 Na_2-phosphocreatine, 4 ATP-Mg, 0.3 GTP, pH 7.3 with CsOH. The bath solution was supplemented with 1 μM TTX, 1 mM 4-AP, and 40 mM TEA-Cl to suppress voltage-gated sodium and potassium currents. Calyx terminals were visualized by oblique illumination (Dodt gradient contrast) through a 60 × water-immersion objective using an upright BX51WI microscope (Olympus). All experiments were performed at RT. The size of the readily-releasable pool of SVs was estimated by monitoring ΔC_m using the sine + DC technique (Lindau and Neher, 1988) using the software lock-in amplifier implemented in PatchMaster (HEKA Elektronik) by adding a 1 kHz sine-wave voltage command (peak-to-peak amplitude ± 35 mV) to V_h = −80 mV. Presynaptic recordings with a leak current > 200 pA were excluded from the analysis. In eEPSC train recordings and during recordings of eEPSC recovery from depression, $\geq$ 3 repetitions per protocol were recorded for each cell included in the final analysis.

Whole-cell patch-clamp recordings from hippocampal CA1 pyramidal neurons were made at RT with patch-pipettes (open-tip resistance 2.5–3.5 MΩ) filled with a solution containing (in mM): 130 K-gluconate, 10 KCl, 2 $MgCl_2$, 2 Na_2ATP, 10 HEPES, 10 EGTA, pH 7.3 with KOH. During experiments, slices were continuously perfused with normal aCSF solution containing 1 mM $MgCl_2$ and 2 mM $CaCl_2$, supplemented with 25 μM bicuculline methiodide (HelloBio) to block $GABA_A$R-mediated IPSCs. Schaffer collateral/commissural fibers were stimulated with a glass electrode filled with aCSF and placed in stratum radiatum $\geq$ 80 μm away from the cell body. Transmitter release was evoked by applying brief electrical pulses (100 μs, 10-50 V). Stimulus intensity was adjusted to obtain peak EPSC amplitudes in the range of 80-300 pA (mean values 161 ± 18 pA, n = 13, and 172 ± 23 pA, n = 13, for wt_{KW} and mut_{KW} synapses, respectively) when stimulated with single APs. Assuming a mean unitary EPSC amplitude of 10-20 pA, this corresponds to the recruitment of 4-30 Schaffer collateral/commissural fibers.

Ca^{2+} Imaging in Nearly Unperturbed Terminals

For measuring AP-evoked Ca^{2+} transients in nearly unperturbed calyces, terminals were preloaded with the low affinity Ca^{2+} dye Cal520-FF (K_d = 9.8 μM). Presynaptic patch pipettes were filled with a K-gluconate based solution containing (in mM): 100 K-gluconate, 60 KCl, 10 HEPES, 5 EGTA, 5 Na_2-phosphocreatine, 4 ATP-Mg, 0.3 GTP, pH 7.3 with KOH, to which 400 μM Cal520-FF were added from stock solution stored at −20°C. Calyx terminals were visualized by oblique illumination (Dodt gradient contrast) through a 60 × water-immersion objective (NA = 1.0) using an upright BX51WI microscope (Olympus). To preload calyx terminals with a final concentration of ~200 μM Cal520-FF, the whole-cell recording configuration was established for a short period of 40–60 s during which the presynaptic firing reliability was tested by eliciting calyceal APs by afferent fiber stimulation using a single stimulus, a 100 Hz train (25 stimuli) and a 200 Hz train (50 stimuli). Presynaptic APs were recorded in the current-clamp mode of the EPC-10 after carefully adjusting the fast-capacitance cancellation in cell-attached mode. Thereafter the pipette was gently retracted to preserve the cytosolic environment. The Ca^{2+} indicator dye was excited at 490 nm using a custom-built LED light source. Fluorescent images were collected at a rate of 100 frames per s with a Grasshopper3 camera (CMOS, FLIR, Germany). The imaging hardware was controlled by Micro-Manager 2.0 software.

QUANTIFICATION AND STATISTICAL ANALYSIS

Time series image stacks were analyzed offline using ImageJ (Schneider et al., 2012) and Igor Pro (Wavemetrics). Offline analysis of electrophysiological data was performed using Igor Pro, R (R Project for Statistical Computing) or Microsoft Excel. Voltage-clamp errors caused by remaining uncompensated Rs were fully compensated by applying a software correction procedure similar to that described in Traynelis (1998) and courtesy provided by E. Neher.

Statistical analysis was conducted using Igor Pro, R and Microsoft Excel. Data are expressed as mean ± standard error of the mean (SEM). Error bars in all graphs indicate SEM. SEM and 95% confidence intervals for *FRP* and $\bar{p}$ estimates derived from eEPSC trains (see below) were obtained by bootstrap resampling analysis using a balanced bootstrap approach (every experimental observation appeared exactly the same number of times in the total population of 10,000 bootstrap samples) (Davison et al., 1986; Gleason, 1988). If not stated otherwise, a two-tailed Welch–Satterthwaite t test was used to test for statistical significance of differences between sample means (see p values in Table S1). In Table S1, the number of animals used in each experiment is indicated by a capital N, whereas the number of cells tested is indicated by a lowercase n.

eEPSC Trains and Paired-Pulse Ratios (PPR)

For a train of presynaptic APs, the prediction of a simple depletion model featuring a constant SV recruitment rate constant $k_+ = \frac{1}{\tau_r}$ for the number of occupied sites N_i immediately before arrival of the $i+1^{th}$ AP can be calculated recursively according to

$$N_{i+1} = (1-p_i) \times N_i + (N_{total} - (1-p_i) \times N_i) \times \left(1 - e^{-\frac{\Delta t}{\tau_r}}\right); \text{for i} \geq 1$$

where N_{total} is the sum of all docking sites, p_i is the release probability at AP arrival, Δt is the inter-stimulus interval, and τ_r is the time constant of recovery.

For simplicity, we assume here $N_1 = N_{total}$.

Assuming that p increases immediately following an AP from its current value by a constant fraction a toward a maximum value of 1, we can express p_i recursively as

$$p_{i+1} = (p_i + a \times (1 - p_i) - p_0) \times e^{-\Delta t/\tau_f} + p_0; \text{for i} \geq 1$$

$$p_1 = p_0$$

where p_0 is the release probability at rest, τ_f is the time constant of synaptic facilitation, and Δt is the inter-stimulus interval.

For the paired-pulse ratio (PPR) of the first two consecutive eEPSCs we can therefore write

$$PPR = \frac{EPSC_2}{EPSC_1} = \frac{N_2 \times p_2}{N_1 \times p_1} = \left(1 - p_0 \times e^{-\frac{\Delta t}{\tau_r}}\right) \times \left(1 + b \times e^{-\frac{\Delta t}{\tau_f}}\right); b = a \times \left(\frac{1}{p_0} - 1\right)$$

Readily-Releasable SV Pool and Release Probability

The whole entity of SVs that can be released within about 50 ms in response to strong and prolonged presynaptic $[Ca^{2+}]_i$ elevations elicited by presynaptic Ca^{2+} uncaging or direct presynaptic depolarizations can be subdivided into two main SV subpools – 'fast releasing' (*FRP*) and 'slowly releasing' (*SRP*) SVs. The *SRP* only marginally contributes to AP-evoke release (Sakaba, 2006) such that pool estimates derived from AP-evoked eEPSCs primarily represent the *FRP*. There is good experimental evidence showing that the *FRP* itself is functionally inhomogeneous (Lee et al., 2013; Taschenberger et al., 2016). For simplicity, we neglect such functional heterogeneity of the *FRP* here and report average *p* values ($\overline{p}$) instead. Assuming, for example, that the *FRP* of calyx terminals is composed of two population of SVs having different *p*, we can write

$$EPSC = q \times N \times \overline{p} = q \times (N_{high} \times p_{high} + N_{low} \times p_{low}) = q \times N \times \left(\frac{N_{high}}{N} \times p_{high} + \frac{N_{low}}{N} \times p_{low}\right)$$

where N is the sum of occupied sites $N_{high} + N_{low}$, q is the quantal size and the subscripts identify high- and low-p release sites. In this case, $\overline{p}$ is simply a weighted average

$\overline{p} = \frac{N_{high}}{N} \times p_{high} + \frac{N_{low}}{N} \times p_{low}$. During train stimulation, N_{high} decreases more rapidly than N_{low} because $p_{high} > p_{low}$. This causes $\overline{p}$ to decrease. This decrease is partially compensated by synaptic facilitation. For simplicity, we assume here that $\overline{p}$ remains approximately similar throughout the trains.

We obtained an estimate for the FRP from cumulative eEPSCs measured in response to high-frequency trains (50, 100 and 200 Hz). The cumulative eEPSC amplitude was corrected for SV recruitment by fitting a line to the final 4 eEPSCs representing the steady state ($eEPSC_{ss}$) and back-extrapolating that line to $eEPSC_1$ (Neher, 2015; Schneggenburger et al., 1999). Such approach rests on the assumptions that (*i*) all release at steady state is balanced by SV replenishment which occurs at constant rate throughout a stimulus train and that (*ii*) the FRP is fully emptied after each AP under steady-state conditions. Neither of these two conditions is fully met: SV replenishment – the product of replenishment rate constant k_+ and number of empty docking sites N_e – operates at considerably higher rate at steady state in comparison to the onset of the stimulus train because: (*i*) k_+ is upregulated during train stimulation and (*ii*) N_e is still low at the beginning of stimulation but increases during ongoing stimulation. In addition, stimulation protocols featuring high frequency AP trains are unlikely to deplete the *FRP* completely and therefore the back-extrapolation approach measures only the depleted fraction of the *FRP* (for discussion see Neher, 2015).

Thus, the back-extrapolation approach is expected to underestimate the actual *FRP* size. We confirm this by observing that *FRP* estimates obtained at 50 and 100 Hz stimulation were consistently lower than those obtained at 200 Hz stimulation. We therefore refer to such estimates as apparent pool sizes FRP'_{50Hz}, FRP'_{100Hz} and FRP'_{200Hz}. When plotting $1/FRP'$ for 50, 100 and 200 Hz as a function of $1/f_{stim}$, where f_{stim} is the stimulation frequency, we notice that this relationship is nearly linear and we can therefore obtain a corrected estimated FRP_{corr} for the case $\frac{1}{f_{stim}} = 0$ s by linear regression as the inverse of intercept of such regression line with the abscissa (Figures 4B and S5C).

Steady-State Replenishment Rate Constant ($\overline{k}_+$)

At steady state, the average rate of release is balanced by the average rate of replenishment $r_- = r_+$, with $\overline{r}_- = N_{ss} \times \overline{p} \times f_{stim}$ and $\overline{r}_+ = (N_{total} - \overline{N}_{ss}) \times \overline{k}_+$, where N_{total} is the total number of sites (occupied or empty), N_{ss} is the number of occupied sites at steady state immediately before AP arrival, and $\overline{N}_{ss}$ and $\overline{k}_+$ are the average number of occupied sites and the average replenishment rate constant

during the inter-stimulus interval at steady state, respectively. For high-frequency stimulation that leads to strong SV pool depletion, a majority of docking sites is empty such that the difference between N_{ss} and $\overline{N}_{ss}$ is negligible in comparisons to the number of empty sites $\overline{N}_{total} - \overline{N}_{ss}$ and we can write $\overline{k}_+ \approx N_{ss}/(N_{total} - N_{ss}) \times \overline{p}_{ss} \times f_{stim}$.

With $EPSC_1 = N_{total} \times \overline{p}_1 \times q$ and $EPSC_{ss} = N_{ss} \times \overline{p}_{ss} \times q$, and if we further assume that $\overline{p}_{ss} \approx \overline{p}_1$, then we obtain $\overline{k}_+ \approx EPSC_{ss} \times f_{stim} \times \frac{EPSC_1}{FRP_{corr} \times (EPSC_1 - EPSC_{ss})}$. $\overline{k}_+$ is accurate only within the limits of the simplifications described above but nevertheless serves as a useful parameter for comparing the functional differences among C_2BDN, C_2BKW and WR mutant mice.

STP at Hippocampal SC/C-CA1 Synapses

Synaptic responses (R) at SC/C-CA1 synapses were modeled as being proportional to the product of a depletable resource (N) and a probability by which this resource is consumed by an AP (p):

$$R_i \sim N_i \times p_i$$

Postsynaptic sensitivity to glutamate (q) was assume to be invariant. All eEPSC train amplitudes were normalized to the respective peak amplitude of the first eEPSC during the conditioning 10 Hz stimulus trains. Changes in synaptic strength during conditioning trains and during subsequent recovery from depression were simulated using a simple model considering depletion of N and a slowly decaying augmentation of p. A contribution of fast decaying paired-pulse facilitation was small under our experimental conditions and therefore neglected. The magnitude of N immediately before arrival of the i+1th AP was calculated according to:

$$N_{i+1} = (1 - p_i) \times N_i + (N_{total} - (1 - p_i) \times N_i) \times \left(1 - e^{-\frac{\Delta t}{\tau_r}}\right)$$

$$p_{i+1} = (p_i + a \times (1 - p_i) - p_0) \times e^{-\frac{\Delta t}{\tau_a}} + p_0; \text{for i} \geq 1$$

$$N_1 = N_0$$

where N_0 designates the resting value of N which for the analysis shown in Figure 8H equates to $1/p_1$ because of the normalization of all R_i relative to R_1, p_i is the release probability at arrival of the ith AP, Δt is the inter-stimulus interval, and τ_r is the time constant of N. Assuming that p increases immediately following an AP from its current value by a constant fraction a toward a maximum value of 1, we can obtain p recursively as:

$$p_{i+1} = (p_i + a \times (1 - p_i) - p_0) \times e^{-\frac{\Delta t}{\tau_a}} + p_0; \text{for i} \geq 1$$

$$p_1 = p_0$$

where p_0 is the resting value of p, τ_a is the decay time constant of augmentation, and Δt is the inter-stimulus interval. Fit results for p_0 and a were 0.06 and 0.002 in wt_{KW} and 0.08 and 0.003 in mut_{KW} synapses, respectively. The time constant of augmentation τ_a amounted to ~9 s for both wt_{KW} and mut_{KW} synapses.